

Upper Mantle Structure beneath the Contiguous US Resolved with Array Observations of SKS Multipathing and Slowness Vector Perturbations

J. Ward¹, M. Thorne², A Nowacki¹, S. Rost¹

¹School of Earth and Environment; University of Leeds
Department of Geology and Geodetics; University of Hull

¹School of Earth and Environment; University of Leeds
²Department of Geology and Geophysics; University of Utah

Key Points:

- We present the first continent-scale analysis of slowness vector deviations, slowness vector divergence, and multipathing.
 - We resolve seismically slow and fast structures such as slabs and hotspots and find tomography model NA13 fits our data best.
 - Slowness vector measurements are vital to study the Earth's mantle and we argue should be included in tomography inversions.

Corresponding author: James Ward, J.Ward2@leeds.ac.uk

14 Abstract

15 Continent-scale observations of seismic phenomena have provided multi-scale con-
 16 straints of the Earth's interior. Of those analysed, array-based observations of slowness
 17 vector properties (backazimuth and horizontal slowness) and multipathing have yet to
 18 be made on a continental scale. Slowness vector measurements give inferences on man-
 19 tle heterogeneity properties such as velocity perturbation and velocity gradient strength
 20 and quantify their effect on the wavefield. Multipathing is a consequence of waves in-
 21 teracting with strong velocity gradients resulting in two arrivals with different slowness
 22 vector properties and times. The mantle structure beneath the contiguous United States
 23 has been thoroughly analysed by previous seismic studies and is data-rich, making it an
 24 excellent testing ground to both analyse mantle structure with our approach and com-
 25 pare with other imaging techniques. We apply an automated array-analysis technique
 26 to an SKS dataset to create the first continent-scale dataset of multipathing and slow-
 27 ness vector measurements. We analyse the divergence of the slowness vector deviation
 28 field to highlight seismically slow and fast regions. Our results resolve several slow man-
 29 tle anomalies beneath Yellowstone, the Appalachian mountains and fast anomalies through-
 30 out the mantle. Many of the anomalies cause multipathing in frequency bands 0.15–0.30
 31 and 0.20–0.40 Hz which suggests velocity transitions over at most 500 km exist. Com-
 32 paring our observations to synthetics created from tomography models, we find model
 33 NA13 (Bedle et al., 2021) fits our data best but differences still remain. We therefore
 34 suggest slowness vector measurements should be used as an additional constraint in to-
 35 mographic inversions and will lead to better resolved models of the mantle.
 36

Plain Language Summary

37 Observations of many phenomena such as reflections and scattering of waves gen-
 38 erated by earthquakes have been analysed on a continental scale. These observations have
 39 lead to great progress in our understanding of the Earth's structure and dynamics. What
 40 has yet to be analysed on such a large scale are the deflections of seismic waves at the
 41 boundaries of structures such as mantle upwelling. Analysing these deflections can give
 42 information on the boundary structure of mantle structures. In this study, we present
 43 the first continent-scale dataset of measurements quantifying the extent waves have been
 44 perturbed from their path between earthquake to recording station. From this new dataset,
 45 we infer the extent of the deflection is dependent on the spatial scale we are sensitive to.
 46 When analysing our dataset spatially, we find evidence for several potential mantle up-
 47 wellings and fragmented subducted crust beneath the US. Our observations support pre-
 48 vious models of the upper mantle beneath the US but differences remain suggesting ob-
 49 servations of direction and velocity could improve the creation of these models. Our ob-
 50 servations show mantle structure can be well resolved with measurements of wavefield
 51 deflection and that these measurements will be crucial for furthering our understand-
 52 ing of Earth structure and dynamics.

1 Introduction

53 Seismic phenomena analysed on a continental scale have improved our understand-
 54 ing of whole-Earth dynamics. Such studies have analysed reflectors in the mid mantle
 55 (e.g., Deuss et al., 2006; Deuss, 2009; Waszek et al., 2018; Bentham et al., 2017), con-
 56 verted phases (Abt et al., 2010; Jenkins et al., 2017), and small-scale heterogeneity from
 57 scattering (Hedlin & Shearer, 2000; Waszek et al., 2015; Ma & Thomas, 2020), from wave-
 58 form complexity (Thorne et al., 2020, 2021), and through seismic tomography (Fichtner
 59 et al., 2018; Bedle et al., 2021; Sigloch et al., 2008; Schmandt & Lin, 2014). Using slow-
 60 ness vector measurements (backazimuth and horizontal slowness) to quantify diffraction
 61 and observe multipathing caused by mantle heterogeneity boundaries has yet to be per-
 62 formed on a continental scale. Diffraction and multipathing are sensitive to the veloc-
 63

ity gradient strength and velocity perturbations of the heterogeneity. As seismic velocity changes with both temperature and composition, these observations can give insight into the thermal and compositional gradients at the boundaries of these anomalies, and be used to test geodynamical hypotheses. Multipathing occurs when a wavefield is incident on a sufficiently strong velocity gradient that, over a short distance (100s km), the wave travels at different speeds and will be diffracted. This results in multiple distinct arrivals each with different arrival times and, because of the diffraction, with different horizontal velocities and directions (horizontal slownesses and backazimuths). Multipathing has been observed in slowness space in surface waves (Maupin, 2011) and body waves (Ward et al., 2020) and its effect on waveform complexity has been extensively studied (Ni et al., 2002; Ni & Helberger, 2003; Sun et al., 2009; C. Zhao et al., 2015; Sun et al., 2019).

As slowness vector measurements of diffraction and multipathing have not been analysed on a continental scale, we present the first study analysing these phenomena using data sampling the mantle beneath the contiguous United States (US). The contiguous US has been studied intensely using travel-time (Sigloch et al., 2008; Schmandt & Lin, 2014; Shen & Ritzwoller, 2016) and full-waveform tomography (Yuan et al., 2014; Krischer et al., 2018; Rodgers et al., 2022; Zhou et al., 2022) as well as higher resolution studies using scattering (Ritsema et al., 2020), structure beneath seismic arrays (Capon, 1974) and receiver functions (e.g., Abt et al., 2010; Schmandt et al., 2014; Kind et al., 2015). These studies have shown the upper mantle is complex with the possible presence of mantle plumes (Schmandt & Humphreys, 2010; Tian et al., 2009; Porritt et al., 2014; Tao et al., 2020) and lithosphere fragments (Sigloch et al., 2008; Tian et al., 2011; Pierce & Morgan, 2009; Bunge & Grand, 2000; Grand et al., 1997; Biryol et al., 2016; Wang et al., 2019). The contiguous US has an abundance of data, has been heavily studied and has complex mantle structure. Therefore, it is an excellent location to perform the first continental-scale analysis of mantle structure using slowness vector measurements and multipathing. We do this with minimal need for visual inspection by applying the automated array technique of Ward et al. (2021) to a continental-scale SKS dataset taken from Thorne et al. (2020), densely sampling beneath the US.

We perform the analysis over three frequency bands each sensitive to different length scales and make 5960 observations (Table S1). We first analyse the frequency dependence of multipathing observed by Ward et al. (2020) and slowness vector deviation magnitude, and then analyse the dataset spatially. Forward modelling results show fast seismic anomalies cause slowness vector deviations to have a converging pattern and a slow seismic anomaly to have a diverging pattern (see Section 4.1). Therefore, we analyse slowness vector deviations by taking the divergence to highlight regions of fast or slow mantle heterogeneities. We observe slowness vector deviations indicative of fast and slow anomalies in the North American upper mantle possibly caused by subducted slab fragments, the Yellowstone anomaly and the Northern Appalachian Anomaly. We find multipathing is present at the boundaries of many heterogeneities in the highest frequency band (0.20–0.40 Hz) and anomalies that have been interpreted as lying between the 410 and 660 transition zone depths show multipathing strongly in the 0.15 – 0.30 Hz frequency band. Future work can focus on exploring the relationship between frequency dependence of multipathing and stagnating slabs as well as the incorporation of slowness vector measurements into tomographic inversions.

2 Methods

2.1 Data and Sub-Arrays

We used a subset of the global SKS dataset of Thorne et al. (2020), which included events between 1990 and 2017 with magnitudes greater than 5.8, deeper than 75 km and with epicentral distances between 90° and 130°. SKS has several advantages to study

mantle structure. As shown in our modelling later, source-side mantle structure has little effect on the slowness vector measurement. The outer core is assumed to be well mixed and have a radial seismic structure so it should not affect slowness vector measurements. SKS has a near vertical incidence, therefore when interpreting the results, one can assume a wave exits the core and travels steeply through the mantle, making SKS sensitive to lateral velocity gradients. A disadvantage of using SKS is it is challenging to infer the depth or depth extent of the heterogeneities we find. In the future, using other phases with other incidence angles in combination with SKS may constrain heterogeneity depths better.

The raw data were processed as described in Thorne et al. (2020) by removing the mean and trend then the instrument response. Low-quality data were removed first with an ensemble of neural networks each trained on the amplitude spectra of 10,000 traces and their respective labels of high or low quality following the approach of Valentine and Woodhouse (2010). Following this, all traces were visually inspected for quality and the high-quality traces were kept for analysis. For each event, the stations recording high-quality data were divided into sub-arrays using the following approach.

To ensure high-quality observations, we required a sub-array to have a minimum of 15 stations with a maximum aperture of 400 km. To ensure all sub-arrays met these criteria, we first used density-based clustering algorithm DBSCAN (Ester et al., 1996) to remove stations which do not meet the criteria defined above. DBSCAN (Ester et al., 1996) is a density-based clustering algorithm that classified the station locations into ‘core’ stations, which have at least 15 other stations within 200 km of it, ‘boundary’ stations which did not meet the density criteria but are within the 200 km neighbourhood of a core station and ‘outlier’ stations which did not meet the density criteria and were not in the 200 km neighbourhood of a core station. The outlier stations were removed and not used to make sub-arrays. We spatially resampled the core stations such that none were within 200 km of each other. This was done by randomly selecting a core station, recording it as a centroid station, removing all core stations within 200 km of it and randomly moving to another core station. This continued until all stations are centroid stations or removed as candidates to be centroid stations. For each of the centroid stations, we created a sub-array made up of all stations within 200 km of it. Figure S1 illustrates the steps to form sub-arrays and Figure 1 shows the resulting sub-array locations with the events and sampling of SKS in the lower mantle.

2.2 Automatic multipathing and slowness vector measurements

For each event–sub-array combination, we used the method of Ward et al. (2021) to automatically identify multipathed and single arrivals in slowness space and measure their slowness vector properties. Here, we provide a brief summary of the method but for details, such as searching for optimal parameters, see Ward et al. (2021).

The waveforms recorded at a seismic array from which the measurement is to be made are bootstrap sampled (Efron, 1992) into N (1000 here) sub-samples. For each of the N bootstrap samples, we use beamforming (Rost & Thomas, 2002) corrected for a curved wavefront (Ward et al., 2020) to calculate the coherent power at a range of slowness vector properties. From this power distribution in slowness-space, take the top M power maxima (3 here) above a noise estimate. The location of the maxima in slowness space gives their slowness vector properties. For the sake of ease of explanation, we describe slowness vector properties as points in a 2-D slowness-space. Each bootstrap sample will have its own power distribution and respective points. Gather all points from each of the bootstrap samples and use DBSCAN (Ester et al., 1996), to identify arrivals as dense clusters of the points. DBSCAN parameters ϵ and $MinPts$ define the density threshold to identify the clusters where at least $MinPts$ points need to be within a radius ϵ for a region to be defined as a cluster. We set the DBSCAN parameters ϵ and $MinPts$

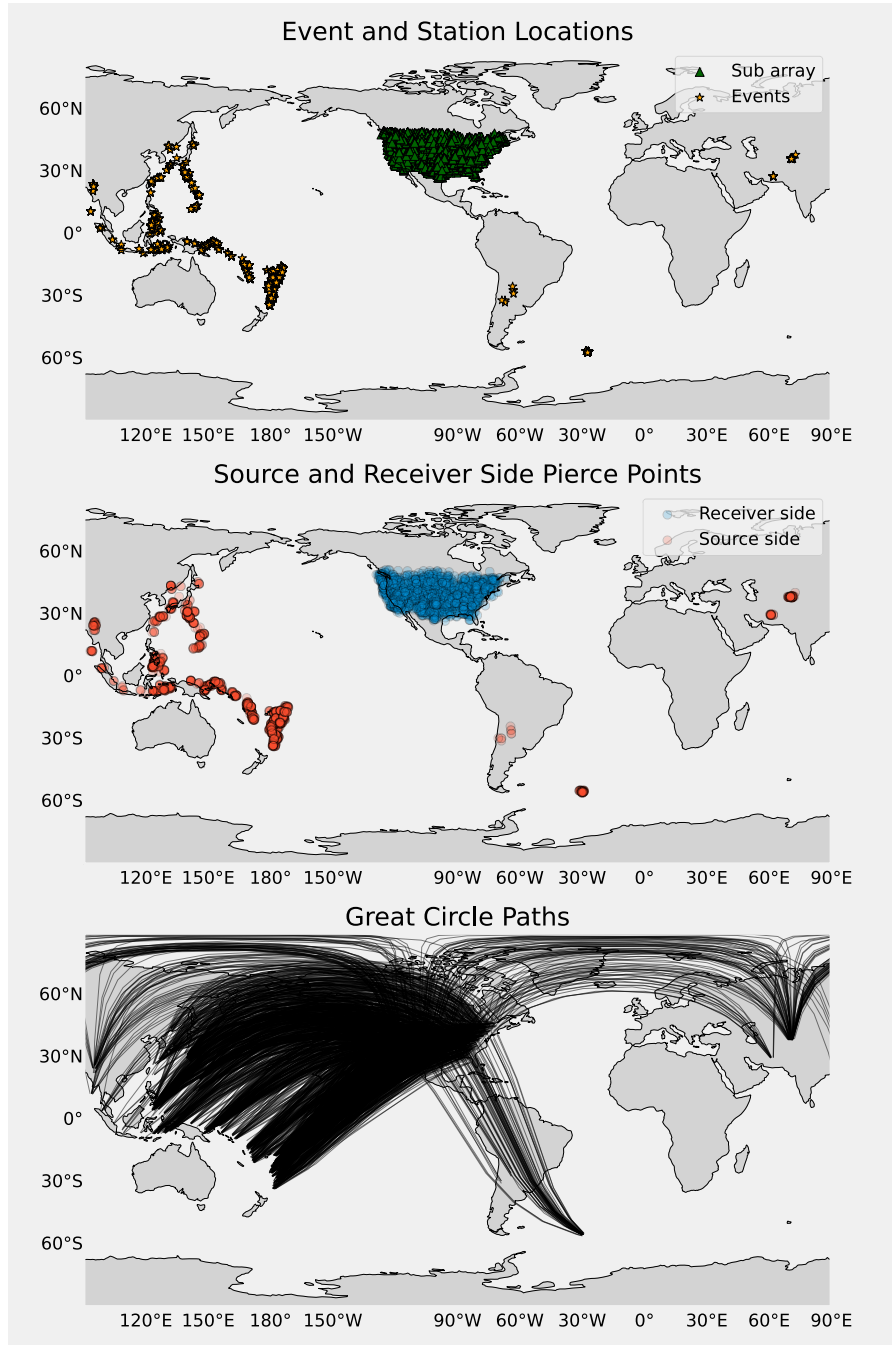


Figure 1. Top: Event (orange stars) and sub-array (green triangles) coverage of the high-quality observations after applying the method from Ward et al. (2021). Middle: map of SKS pierce point coverage at 2800 km depth for the observations after applying the method of Ward et al. (2021). Blue and red circles show the pierce point location on the receiver- and source-side, respectively. Bottom: great circle paths from event to stations.

as 0.20 s/ $^{\circ}$ and 250 points respectively in line with the tuning from Ward et al. (2021). The number of clusters found is taken as the number of arrivals, the mean of the location of the points in each cluster gives the slowness vector properties of the arrival and the scatter of the points in each cluster gives the uncertainty estimates of the slowness vector measurement. Figure S2 illustrates the method.

By using this method, we can confidently make slowness vector measurements of a large dataset and identify multipathing. We define multipathing as more than one SKS arrival being found within the 40 second time window by the method outlined above and be within 3 s/ $^{\circ}$ of the PREM predicted slowness vector properties. Observations classified as multipathed were visually inspected to check the classification and if necessary relabeled. Multipathing from lower mantle structure has been observed to be frequency-dependent (Ward et al., 2020) suggesting the Fresnel zone size relative to the velocity gradient sharpness of the boundary may impact whether multipathing is observable or not. Therefore, constraining in which frequency band multipathing is observable may give an indication of the velocity gradient sharpness or depths due to the variation of the Fresnel zone with depth as well as frequency. To identify velocity gradients of different sharpness and strength, we conduct this analysis in three frequency bands (0.10 – 0.20 Hz, 0.15 – 0.30 Hz, 0.20 – 0.40 Hz). In total there were 5960 observations. The breakdown of the number of multipathed and single arrivals in each frequency band is shown in supplementary Table S1.

Instead of analysing backazimuth and horizontal slowness deviations, we analysed slowness vector deviations. We define the slowness vector deviation as the vector from the predicted location in slowness space to the observed location as shown in Figure 2. The larger the magnitude of the vector, the further the observation is from the PREM (Dziewonski & Anderson, 1981) prediction.

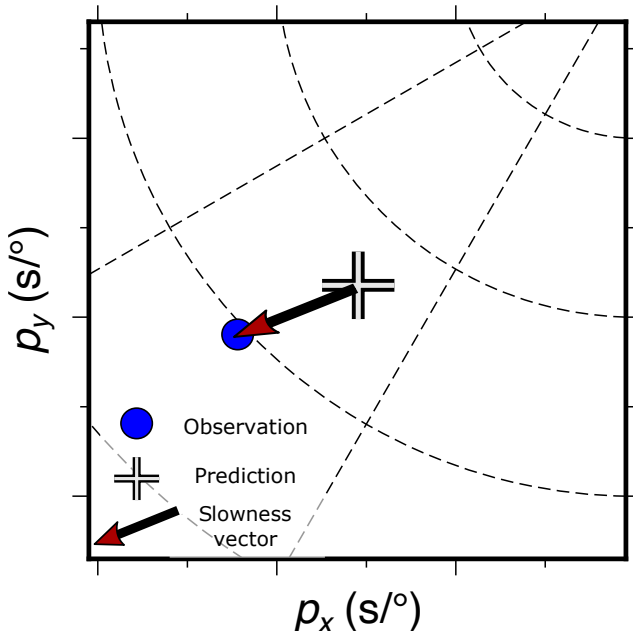


Figure 2. Cartoon illustrating our definition of the slowness vector deviation. p_x is the horizontal slowness in the east-west direction and p_y is the horizontal slowness in the north-south direction. The slowness vector deviation is the vector from the PREM (Dziewonski & Anderson, 1981) predicted arrival location in slowness space (black and grey cross) to the location of the observed arrival (blue circle).

191 **2.3 Constraining velocity gradient depth**

192 A challenge with interpreting SKS slowness vector measurements and multipathing
 193 locations is determining the depth of the structure causing the wavefield perturbations
 194 and whether it is on the source- or receiver-side. Furthermore, interpretation becomes
 195 more complex as there could be multiple structures affecting the wavefield at different
 196 depths and locations. The unique sampling density we are able to achieve in this dataset
 197 allows us for the first time to attempt to constrain the depth and location (source or re-
 198 ceiver) of heterogeneities with the following approach.

199 For this analysis, assuming there is a single dominant structure causing the per-
 200 turbation, we assume waves that sample similar regions should arrive with a similar slow-
 201 ness vector deviation as defined in Figure 2. The backazimuth and horizontal slowness
 202 deviations will vary with sampling azimuth but the vector which describes the full slow-
 203 ness vector deviation, as shown in Figure 2, will not. This is because the slowness vec-
 204 tor deviation is orthogonal to the velocity gradient that causes the wave to diffract re-
 205 gardless of the sampling azimuth as we show later through forward modeling in Section
 206 4.1. We quantified the similarity of slowness vector deviations of all observations sam-
 207 pling within 200 km bins by calculating their variance. The variance (σ^2) of the slow-
 208 ness vector measurements is calculated as the mean square distance between all the slow-
 209 ness vectors and the mean as

$$\sigma^2 = \frac{\sum_i^N (\sqrt{(\bar{p}_x - p_{ix})^2 + (\bar{p}_y - p_{iy})^2})^2}{N}, \quad (1)$$

210 where N is the number of vectors in the bin, \bar{p}_x and \bar{p}_y are respectively the east and north
 211 components of the mean slowness vector in the bin, and p_{ix} and p_{iy} are respectively the
 212 east and north components of the i^{th} slowness vector measurement in the bin. The dis-
 213 tances between the mean slowness vector and each of the slowness vector measurements
 214 are illustrated in Figure S3. When calculating the variance, we relocated the pierce point
 215 from its great circle path to the location it would travel from such that it arrived with
 216 the observed backazimuth and horizontal slowness (Ward et al., 2020).

217 We identified depths where mantle heterogeneities may be present by calculating
 218 the number of bins with a statistically significantly low variance. We did this by project-
 219 ing the slowness vector measurements along their theoretical ray path from PREM to
 220 the depth in question, taking all observations within 100 km of the bin centre, and cal-
 221 culating the variance of the measurements in each bin as described in Equation 1. To
 222 infer which variances are statistically significantly low, we randomly took 20 slowness
 223 vector measurements from the whole dataset and calculated the variance. This was re-
 224 peated 1000 times and the 5th percentile of these 1000 random variance estimates is recorded.
 225 Variances lower than the 5th percentile estimate are labelled as significantly low and counted
 226 for that depth.

227 We infer which depths are likely to have heterogeneity from histograms of the num-
 228 ber of low-variance bins with depth (Figure 5). From the histogram, we took the depths
 229 with more low-variance bins than the adjacent depths and analysed the slowness vec-
 230 tor deviations spatially. This approach gives an approximation about which depths may
 231 have mantle heterogeneity and attempts to address the poor depth resolution of SKS.
 232 Observations from other phases such as direct S wave arrival should be incorporated in
 233 the future to further improve the depth resolution.

234 The variance analysis could be repeated by analysing the relative slowness vectors
 235 of the multipathed arrivals in the same observations. Different slowness vector proper-
 236 ties would manifest itself as different locations in slowness space and these relative lo-
 237 cations of the multipathed arrivals is indicative of the velocity gradient orientation that
 238 caused them (Ward et al., 2020). The slowness-space locations of the multipathed ar-
 239 rivals can be quantified by the azimuth between the locations in slowness space. If the

same velocity gradient causes the multipathing in several observations, we expect the multipathed arrivals to have similar relative locations in slowness space. We could perform similar variance analysis to that performed earlier on the azimuths between the multipathed arrivals that sample a similar region. We did not do this as most regions show few multipathed arrivals to reliably calculate the variance.

245 2.4 Estimating velocity gradient length scales

246 Once multipathing is observed, we cannot infer properties of the velocity gradient
 247 which caused it without computationally expensive finite-frequency forward modelling.
 248 We can, however, give an upper bound of the length scale of the transition from the am-
 249 bient mantle to the interior of the heterogeneity. When we present our multipathing ob-
 250 servations and discuss possible causes we will give an estimate of the upper bound of the
 251 lateral velocity gradient extent. We do this by calculating the total area the array of sta-
 252 tions is sensitive to in the mantle at the depth from which we hypothesise the multipathing
 253 comes.

254 We calculate the Fresnel zone diameter using

$$d = 2\sqrt{\frac{z\lambda}{2}}, \quad (2)$$

255 where d is the Fresnel zone diameter at depth z . The wavelength λ is calculated from
 256 the lower end of the frequency band in which multipathing has been observed (0.10, 0.15,
 257 or 0.20 Hz) and the PREM (Dziewonski & Anderson, 1981) velocity value at depth z .
 258 To find the upper bound of the velocity gradient length scale, this needs to be added to
 259 the diameter of the sub-array used for the recording, which we set as 400 km (Section
 260 2.1). The diameter to which the array measurement is sensitive will change with depth.
 261 For example, a region spanning 400 km at the surface will become approximately 370 km
 262 when projected to the 410 transition zone. Therefore, this is accounted for before adding
 263 to the diameter of the Fresnel zone. With this, we propose maximum length scales for
 264 the lateral velocity gradients of heterogeneity observed.

265 2.5 Calculating the divergence of the slowness vector field

266 Results of forward modelling (4.1) show the divergence of slowness vector devia-
 267 tions is indicative of whether the velocity anomaly is positive or negative. Therefore, we
 268 calculated the divergence over the grid of binned slowness vectors using

$$\nabla \cdot p = \frac{\delta p_x}{\delta x} + \frac{\delta p_y}{\delta y}, \quad (3)$$

269 where δp_x represents the differential of the east-west slowness vector component (p_x) of
 270 longitudinally adjacent slowness vector bins, δx is the spacing of the slowness vectors with
 271 longitude, δp_y is the differential of the north-south slowness vector component (p_y) of
 272 laterally adjacent slowness vector bins and δy is the latitude spacing. A positive diver-
 273 gence is expected for a low-velocity anomaly and a negative divergence for a high-velocity
 274 anomaly (see Section 4.1).

275 The grid spacing in longitude and latitude is 200 km and we calculated the diver-
 276 gence between the adjacent slowness vector components only. We assume the spacing
 277 between vectors is small enough that the effect of a spherical surface can be ignored. The
 278 divergence is plotted in the background of the slowness vector maps and can be used to
 279 infer the location of fast or slow anomalies. We can not directly relate the magnitude
 280 of divergence to the magnitude of the velocity anomaly, but this could be the basis of
 281 future work.

282 **2.6 Limitations**

283 This work is partly limited by the decisions made to automate the sub-array cre-
 284 ation step and in the cluster analysis parameters used in the method of Ward et al. (2021).
 285 The maximum size of the sub-arrays, the minimum number of stations needed for a sub-
 286 array and the spacing of the sub-arrays will affect the number and distribution of the
 287 sub-arrays. The parameters were chosen such that each sub-array has sufficient stations
 288 to provide reliable observations while maximising the coverage of the mantle without such
 289 heavy sampling that some observations are nearly redundant.

290 The parameters given to the automated method of Ward et al. (2021) to make the
 291 slowness vector measurements and identify multipathing is another limitation. Choos-
 292 ing the parameters requires a balance between finding as many low amplitude arrivals
 293 as possible while minimising the misclassification of noise as arrivals. The parameters
 294 used in this study were taken from the tuning in Ward et al. (2021) which were shown
 295 to agree the most with a human-labeled dataset and are best suited to this automated
 296 task.

297 Another limitation is the size of the bins chosen for the variance analysis and plot-
 298 ting. For the variance analysis, the size of the bin should be on the spatial scale expected
 299 for coherent slowness vector values to exist. A bin size that is too large may include many
 300 slowness vector values and may result in high variance and the removal of those obser-
 301 vations. For plotting, too large a bin size or spacing would lose spatial resolution. For
 302 both the plotting and variance analysis, too small a bin size would mean there may be
 303 too few measurements to form a bin to make reliable variance estimates (here we require
 304 at least 10 values in a bin to use it) limiting the spatial coverage. To choose the bin size,
 305 the smallest bin size was chosen which retained enough coverage over the contiguous US
 306 while still having at least 10 observations per bin.

307 We used a constant time window of 20 s before and after the PREM (Dziewonski
 308 & Anderson, 1981) predicted arrival time which may have led to missing some SKS ar-
 309 rivals if they arrived very abnormally early or late and may have missed some multipathed
 310 arrivals. The time window was chosen to avoid contamination by other arrivals, such as
 311 SKKS. Due to the dense coverage of the data, we do not expect missing some arrivals
 312 in extreme cases will greatly affect our results.

313 **3 Results - frequency dependence of multipathing and slowness vec-
 314 tor perturbation**

315 After processing, we have 5960 observations over three frequency bands of back-
 316 azimuth deviations, horizontal slowness deviations, multipathing presence and slowness
 317 vector deviation (Table S1). The average standard deviations of these measurements are
 318 1.62° and 0.13 s° showing the effects of array aperture, station spacing, and near-surface
 319 heterogeneity have little effect on these observations. In this section, we present these
 320 measurements and describe any patterns present.

321 **3.1 Frequency dependence of multipathing**

322 Frequency dependence of multipathing has been observed previously with array meth-
 323 ods by Ward et al. (2020) and was interpreted as a result of different velocity contrasts,
 324 spatial scales or depths. In our observations, we observe clear frequency dependence of
 325 multipathing (Figure 3) with the most multipathing observed in the highest frequency
 326 band and the least multipathing observed in the lowest frequency band. From this, we
 327 infer that velocity gradients on a relatively short spatial scale are more common in the
 328 US mantle. The precise length scale of the velocity gradient will be depth-dependent.
 329 We can give a maximum spatial scale for these velocity gradients at a given depth by

330 calculating their Fresnel zone diameter over the whole sub-array (see Section 2.4). For
 331 velocity gradients in the upper mantle, where we hypothesise most multipathing is tak-
 332 ing place due to the high number of low variance bins in the upper mantle, we suggest
 333 the maximum scale for the velocity gradient could be approximately 500 km, 480 km and
 334 470 km respectively for frequency bands 0.10 – 0.20 Hz, 0.15 – 0.30 Hz and 0.20 – 0.40 Hz.

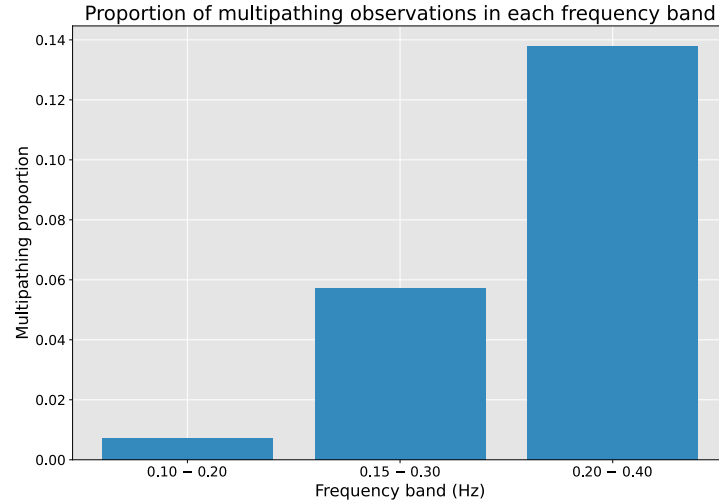


Figure 3. Histogram of the proportion of multipathing observations present in each frequency band. There is a clear trend of more multipathed arrivals observed at higher frequencies.

335

3.2 Frequency dependence of slowness vector deviation magnitude

336 We bin the magnitudes of the slowness vector deviations in 0.1 s/ $^{\circ}$ bins to inves-
 337 tigate whether there is any frequency dependence on slowness vector deviation magni-
 338 tude (Figure 4). We observe evidence for a frequency dependence on slowness vector de-
 339 viation magnitude with more low magnitude slowness vector deviations observed in the
 340 lowest frequency band and more large magnitude slowness vector deviations observed
 341 in the highest frequency band. This pattern could allow broad-scale properties of man-
 342 tle velocity gradients to be constrained if it is replicated through forward modelling stud-
 343 ies.

344

4 Results - Spatial Analysis and Forward Modelling

345 Figure 5 shows the results of the variance-depth analysis (Section 2.3) of the dataset
 346 sampling the mantle beneath the US. There is little evidence for lower-mantle structure
 347 causing slowness vector deviations in our observations in the low and central frequency
 348 bands (0.10 – 0.20 and 0.15 – 0.30 Hz), because there are very few bins with low vari-
 349 ance in the lower mantle suggesting no coherent pattern at this depth. However, the high-
 350 est frequency band (0.20 – 0.40 Hz) contains several regions of high coherency, and as
 351 well as structure at \sim 300 km depth, it appears to be sensitive to mid- and lower-mantle
 352 structure. We identify depths that may have mantle heterogeneity by those which have
 353 a higher number of low-variance bins than surrounding depths in the histograms (Fig-
 354 ure 5). This is best shown in the 0.20–0.40 Hz band in Figure 5, where there are high
 355 bin counts at 400 km, 1300–2000 km and 2800 km depth. The depth slices analysed are
 356 listed in Table 1.

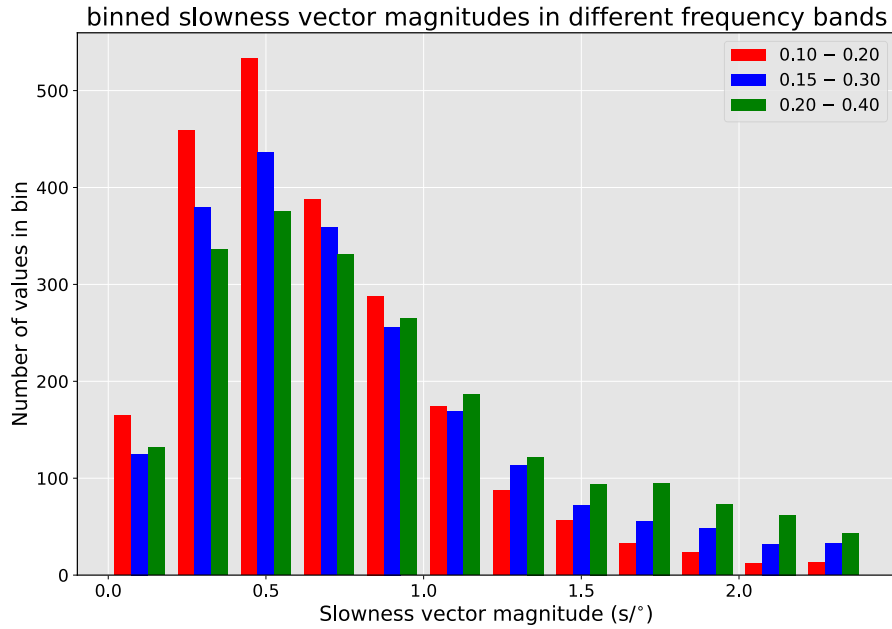


Figure 4. Histogram of slowness vector magnitudes binned in 0.2 s/° bins and coloured by frequency band. There is a clear frequency dependence of slowness vector deviation magnitudes. Lower frequency bands (red) appear to have smaller slowness vector deviations and higher frequency bands (green) appear to have larger slowness vector deviations.

We perform the same variance analysis on the source-side paths of the data. While many bins have significantly low variance, most are low-magnitude slowness vectors ($< 0.5\text{ s/}^\circ$) and are not indicative of sampling mantle heterogeneity.

Frequency band (Hz)	Depths analysed
0.10 – 0.20	200 km, 1000 km, 1800 km, 2000 km
0.15 – 0.30	200 km, 800 km, 1000 km
0.20 – 0.40	300 km, 1800 km, 2891 km

Table 1. Depths with possible mantle heterogeneity inferred from the slowness vector variances.

In the following sections, we first infer what the expected slowness vector deviation observation is for seismically slow and fast heterogeneity. Then, we present our observations at selected depth slices highlighting possible mantle heterogeneity. Following this, our observations are compared to synthetically generated data using three upper mantle tomography models (Schmandt & Lin, 2014; Fichtner et al., 2018; Bedle et al., 2021). This allows us to evaluate the tomography models, our data, and, as these are upper mantle models, the relative contribution of upper and lower mantle heterogeneity to the observations.

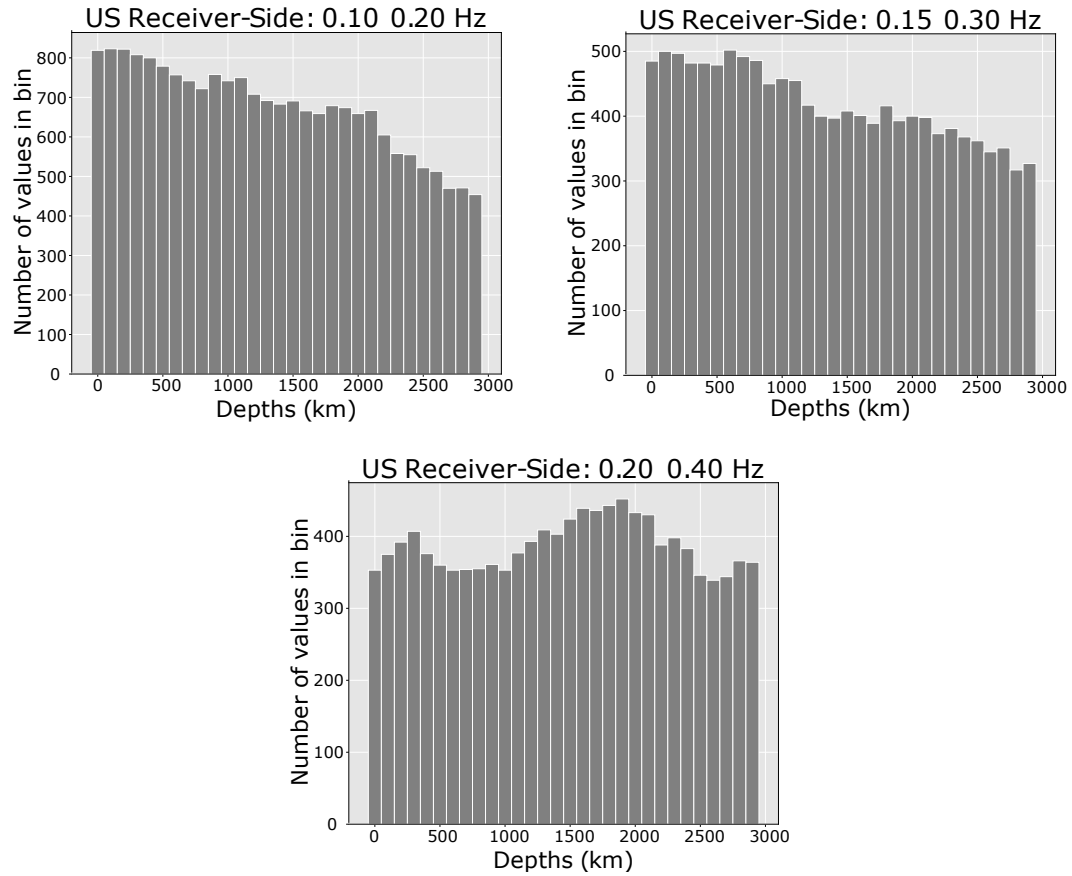


Figure 5. Histograms of the number of bins with a significantly low variance of slowness vector measurements (Section 2.3) at each depth. These have been separated for each frequency band.

368 4.1 Forward modelling tests

369 Before interpreting the observations spatially, we use 3-D ray-tracing (D. Zhao et
370 al., 1992; Simmons et al., 2011, 2012) to infer the qualitative pattern of slowness vec-
371 tor deviations of seismically fast or slow mantle heterogeneity on the scale of 100s of kilo-
372 metres.

373 For a qualitative comparison, ray tracing is sufficient as we do not seek to compare
374 the modelling quantitatively with our observations. The outputs of the ray-tracing ap-
375 proach used here hold no information about the amplitudes of the arrivals, therefore it
376 is unclear if the arrivals will arrive with enough power to be observed. A direct compari-
377 son of the modelling with the data would require finite frequency modelling which is be-
378 yond the scope of this work. Figure S4 shows an example model setup of the anomalies
379 at the CMB with the event and station locations. The fast anomaly has a length of 1000 km
380 east to west, a length of 750 km north to south and a height of 500 km above the CMB,
381 with an S-wave velocity perturbation of +5%. The slow anomaly is a cylinder with a di-
382 ameter of 1000 km, a height of 500 km above the CMB and an S-wave velocity pertur-
383 bation of -5% relative to PREM (Dziewonski & Anderson, 1981). The rest of the model
384 takes the velocities of PREM. To test the effect of velocity anomaly perturbation we vary
385 the anomaly strength to be +2.5 and +10 % for the fast anomaly and -2.5 and -10 %
386 for the slow anomaly. We also test a smaller anomaly with a maximum diameter of 500 km
387 and with an anomaly of +5 and -5 % respectively. For each of these models, we inves-
388 tigate the effect they have when placed on the source and receiver side. We find receiver-
389 side structure has a much greater effect on the slowness vector deviation. We discuss the
390 effects of these further in the supplementary material.

391 We calculate the arrival times at each station and insert a Ricker wavelet (Ricker,
392 1943, 1944) with a frequency of 0.15 Hz at the arrival times creating synthetic seismo-
393 grams. Using the synthetic data, a beamforming grid search is conducted over a range
394 of slowness vectors for each sub-array. We record the slowness vector properties with the
395 highest power value and calculate the deviation from the PREM-predicted slowness vec-
396 tor properties. The differential slowness vector is plotted at the great circle path pierce
397 points between the event and sub-array centre at the CMB. In addition to marking the
398 slowness vector residuals at the great circle path pierce points, the vectors are relocated
399 to the path through which they are inferred to travel in a 1-D Earth, such that they ar-
400 rive with the slowness vector properties as the observation (as in Ward et al., 2020). This
401 allows us to visualise possible origins of the wave after diffraction in the same way as the
402 slowness vector plots in Section 4.2.

403 The slowness vector deviations for both model setups with the relocated locations
404 and the great circle path points plotted are shown in Figure 6. The modelling results clearly
405 show a diverging pattern for the slow anomaly and a converging pattern for the fast anomaly.
406 In both models, the slowness vector azimuths are perpendicular to the orientation of the
407 boundary, are large at the edges of the structure and have a low magnitude in the cen-
408 tre of them. This suggests refraction through the centre of the heterogeneity is not enough
409 to cause slowness vector deviations and that slowness vector measurements are only sen-
410 sitive to the diffraction at the boundaries of the heterogeneities. Larger slowness vector
411 deviation magnitudes are observed for a greater velocity perturbation and smaller de-
412 viation magnitudes for weaker velocity perturbations. For a smaller-sized anomaly, the
413 results suggest the magnitude of the deviations is similar, but the area they are spread
414 over is smaller supporting our interpretation that we are resolving the effects of bound-
415 ary structure.

416 We test the effect of source side structure in our synthetic testing where we use the
417 same anomaly sizes and shapes but find negligible slowness vector deviation magnitudes
418 except in the most extreme case with velocity anomalies of 10 % with a height of 500 km
419 and maximum width of 1000 km. In this case, we find slowness vector deviations of at

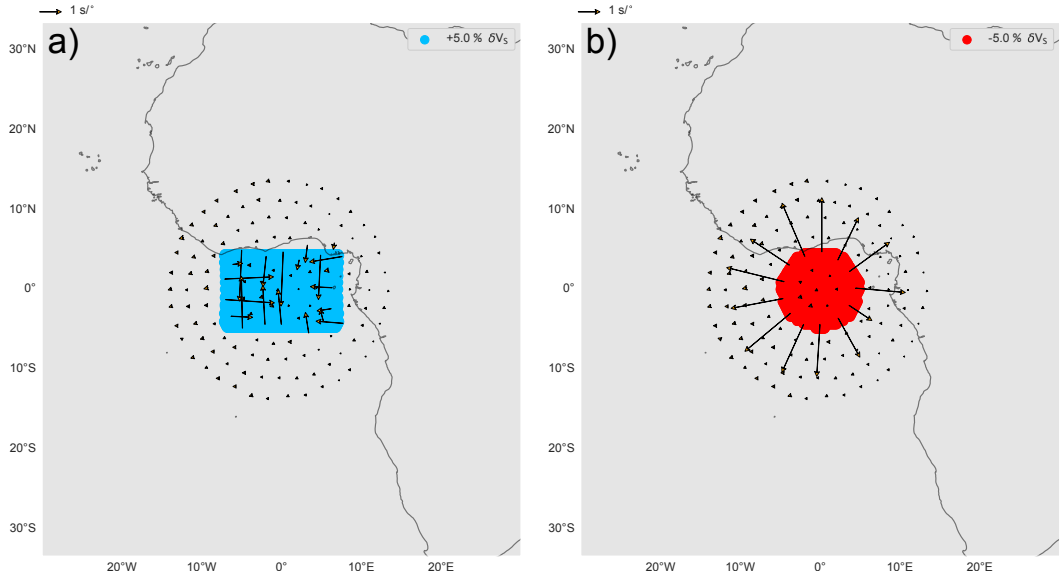


Figure 6. Slowness vector residuals for a fast cuboid (a) and a slow cylinder (b) with model setups shown in Figure S4. The fast cuboid has a depth extent of 300 km from 100 km to 400 km depth, a length of 1500 km and a width of 1000 km and a velocity perturbation of $+5 \delta V_S$. The slow cylinder has a depth extent of 300 km between 100 km and 400 km, a radius of 500 km and a velocity perturbation of $+5 \delta V_S$. Note, the slowness vector patterns for the slow cylinder show a diverging pattern and for the fast box a converging pattern. In all instances, the slowness vector azimuths are orthogonal to the boundary of the structure.

most 0.5 s/°. As this is the most extreme of the test anomaly cases, we do not think source-side structure is contributing significantly to our observations. We discuss this further in the supplementary material in Section S5.

4.2 Spatial observations of slowness vectors and multipathing

Using the results of Section 4.1, we present the slowness vector deviations and multipathing spatially. Multipathing and slowness vector deviation measurements provide different information about the heterogeneity. The presence or lack of multipathing in one or multiple frequency bands constrains the sharpness of the velocity gradient. The relative location of the multipathed arrivals in slowness space may give the orientation of the velocity gradient. It is challenging to recover the velocity anomaly of the heterogeneity through slowness space observations of multipathing alone. Slowness vector measurements on the other hand can give inferences on whether the heterogeneity is seismically fast or slow and the azimuth of the vectors can be used to infer the orientation of the boundary. Therefore, when analysing velocity gradients in the mantle it is important to use both.

We only analyse slowness vector measurements that have a variance lower than the significant variance estimate and are then binned in 200 km-radius bins. The bin size was chosen to maximise clarity while retaining as much detail as possible. The multipathing observations are shown as the proportion of multipathing within 200 km bins with a minimum of 10 observations required to form a bin. Where multipathing is observed, we can estimate the maximum scale of the velocity gradient given the depth and frequency band it is observed in by taking the approach outlined in Section 2.4. To high-

442 light the location of possible heterogeneity, the divergence of the slowness vector field
443 is calculated with the approach discussed in Section 2.5.

444 **445** **4.2.1 Distribution of slowness vector deviations and multipathing beneath the Contiguous US**

446 In this section, we show the spatial distribution of multipathing and slowness vector
447 deviations at selected depths and frequency bands with the remaining depths and
448 frequency bands given in the supplementary material. Possible mantle heterogeneity is
449 highlighted, with a geological interpretation presented later (Section 5). Figures 7 and
450 8 show the observations at 200 km depth and show several regions of strong divergence
451 and high multipathing proportion.

452 We find the strongest positive divergence region (D1, Figure 7a) with large vector
453 deviation magnitude ($>1 \text{ s}^{\circ}$) and moderately high multipathing proportion (40 %; M5
454 in Figure 8a) in the upper mantle beneath the Yellowstone region. Adjacent to the D1
455 anomaly, there are regions of high convergence (C1 and C2). The magnitudes of the slow-
456 ness vectors around C1 vary depending on location with small magnitudes of $< 0.5 \text{ s}^{\circ}$
457 on the west and other regions show large magnitudes of up to 1.5 s° . The C2 anomaly
458 shows more consistent slowness vector magnitudes of approximately 1 s° at all azimuths
459 and is also near a region of high multipathing proportion (50 %) in the central frequency
460 band (M8 in Figure 8b). The M8 anomaly has its highest proportion at depths shallower
461 than 600 km and a much lower proportion deeper in the mantle (Figure 8c). At a depth
462 of 500 km and in the frequency band of 0.15 – 0.30 Hz, we estimate the maximum trans-
463 ition length over which the velocity varies to be 530 km.

464 On either side of the C2 anomaly there are regions of strong positive divergence
465 (D2 and D3) with slowness vector deviations of up to 0.7 s° , suggesting seismically slow
466 material where small-scale upwellings have been hypothesised by some (e.g., Schmandt
467 et al., 2012). These regions show little multipathing, indicating either there are no sharp
468 velocity gradients or they do not have the depth extent to cause multipathing in the slow-
469 ness domain.

470 In the central and eastern US, we observe regions of converging slowness vector resid-
471 uals with low magnitude residuals ($<= 0.2 \text{ s}^{\circ}$) surrounding them. These converging pat-
472 terns (C4 and C5) suggest seismically fast material is present and similar anomalies in
473 other studies have been interpreted as lithospheric fragments (Sigloch et al., 2008; Biryol
474 et al., 2016; Wang et al., 2019). As these regions are not near any diverging patterns we
475 do not think they are an artifact of nearby measurements. These regions have different
476 multipathing characteristics depending on the frequency band. The C4 anomaly shows
477 a high multipathing proportion (60 %, M3 in Figure 8) in both frequency bands which
478 suggests both a large difference in seismic velocities and a short distance over which the
479 change takes place. The C5 anomaly shows some multipathing (40 %, M6 in Figure 8a)
480 near the boundaries of the diverging regions in the highest frequency band only. We in-
481 terpret this as the anomalies boundaries causing multipathing, but the velocity gradi-
482 ent exists on a scale of at most 470 km.

483 In the northeast of the US, we observe a region with diverging slowness vectors (D5)
484 beneath the Appalachian mountains, indicative of seismically slow material. This region
485 does show some multipathing at the boundaries of the diverging region (M7) suggest-
486 ing a transition in terms of temperature or composition on the scale of at most 470 km.
487 We discuss the possible origins of this structure later.

488 West of the D5 anomaly, we observe a sharp change in slowness vector magnitudes
489 from approximately 1 s° to very small deviations giving a negative divergence (C3; Fig-
490 ure 7a). The large slowness vector magnitudes of C3 indicate a lateral velocity gradient
491 or heterogeneity but, as there is a distinct transition to negligible magnitudes, only one

492 strong velocity gradient may be present. The region does show some multipathing in the
493 highest frequency band (M2 in Figure 8a). We speculate this could be the boundary of
494 the North American craton with the transition occurring over at most 470 km.

495 A high multipathing proportion is observed in many regions when the data is pro-
496 jected to 200 km depth but only observed in the higher frequency band (Figure 8a) with
497 very little multipathing observed in the lowest frequency band (Figure 10c). This sug-
498 gests the heterogeneity causing this multipathing is of a sufficiently small scale to only
499 be imaged by the short-wavelength observations. Not all multipathing will be caused at
500 this depth, but we argue a significant proportion will be, because of the high number of
501 low variance bins in the upper mantle (Figure 5). We suggest this multipathing may be
502 caused by structures that are not individually resolvable by seismic tomography or do
503 not cause multipathing in lower frequency bands. We interpret these structures to have
504 velocity gradients with scales of at most 470 km.

505 In the lower mantle (Figure 9), there are regions of diverging slowness vector (D7
506 and D8) which may be indicative of low-velocity structure. However, the effects of up-
507 per mantle structure affecting lower mantle observations mean interpreting the data for
508 lower mantle structure is challenging. We discuss this further in Section 4.3. The wide
509 distribution of high-frequency multipathing in the upper mantle is also observed through-
510 out the lowermost mantle beneath North America (although at a slightly lower propor-
511 tion; Figure 9), but we do not observe large slowness vector magnitudes or patterns in
512 this region. We suggest most of the multipathing is caused by structure in the upper and
513 mid mantle; it is challenging to discern the origin, however.

514 Many depths and frequency bands show a very high proportion (80 %) of multi-
515 pathing which we label M1 in Figure 8, but there is very little slowness vector deviation
516 in either the binned or the unbinned data. We do not know what could be causing such
517 a high multipathing proportion with small slowness vector magnitudes. Future work on
518 a detailed regional analysis to investigate whether combinations of seismically fast and
519 slow mantle structures could lead to these observations or if structures in the near sur-
520 face could be the cause.

521 4.3 Comparison with tomography models

522 Many tomography models have been presented to understand the upper mantle be-
523 neath the US (e.g. Sigloch et al., 2008; Tian et al., 2011; Porritt et al., 2014; Schmandt
524 & Lin, 2014). In this section, we compare our observations to those created by ray trac-
525 ing through three velocity models of the upper mantle to determine how much upper man-
526 tle structure is contributing to our observations and test the tomography models against
527 our observations. Our observations provide a good test for these models as SKS data are
528 not used to make the models and slowness vector measurements are not incorporated
529 into the inversion.

530 We choose the models from Fichtner et al. (2018), Schmandt and Lin (2014) and
531 Bedle et al. (2021) because they use different approaches and data. These velocity mod-
532 els are for the upper to mid mantle only (depths of up to 500–1200 km) and do not con-
533 tain lower mantle structure. For the core and lower mantle, we use velocities from 1D
534 earth model AK135 (Kennett et al., 1995) as this is the reference model used to convert
535 Schmandt and Lin (2014) to absolute velocities and for consistency we use this struc-
536 ture for the other models. We use the same ray tracing software as described in Section
537 4.1 to calculate the travel times for each source-receiver pair in the dataset. We then place
538 a Ricker wavelet at the calculated travel time and use beamforming (Rost & Thomas,
539 2002) to find the slowness vector with the maximum power. From these slowness vec-
540 tor measurements, the same binning process as described earlier is applied.

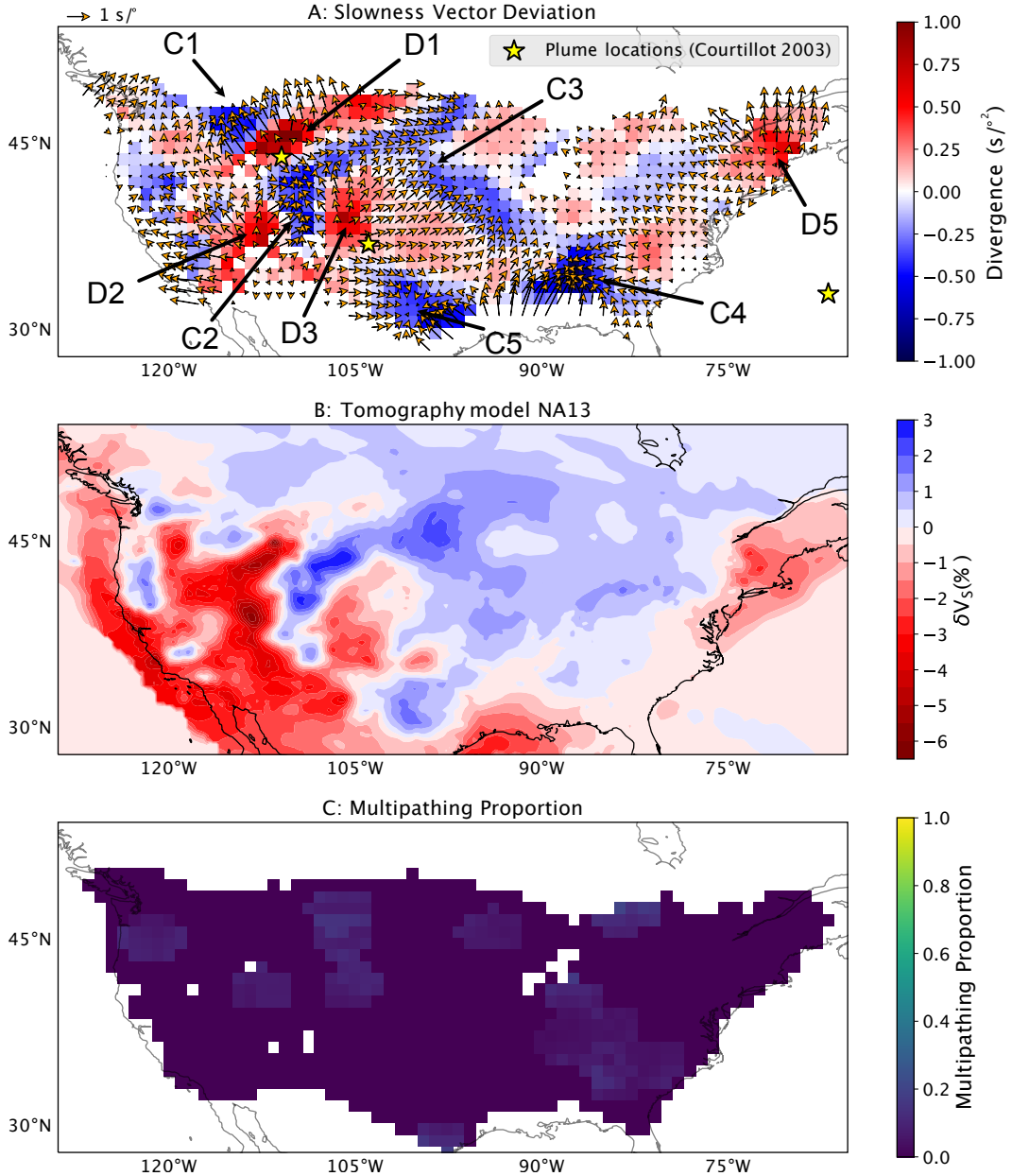


Figure 7. Figure of a) slowness vector deviation bins at 200 km depth with the divergence in the background Plume locations from Courtillot et al. (2003) are shown as yellow stars. The background is the divergence of the slowness deviation vector field calculated using Equation 3. b) velocity structure of tomography model NA13 (Bedle et al., 2021) at 200 km depth, and c) multipathing proportions in the 0.10 – 0.20 Hz frequency band using pierce points at 200 km depth beneath the US. The bins have a radius of 200km with a spacing of 100 km.

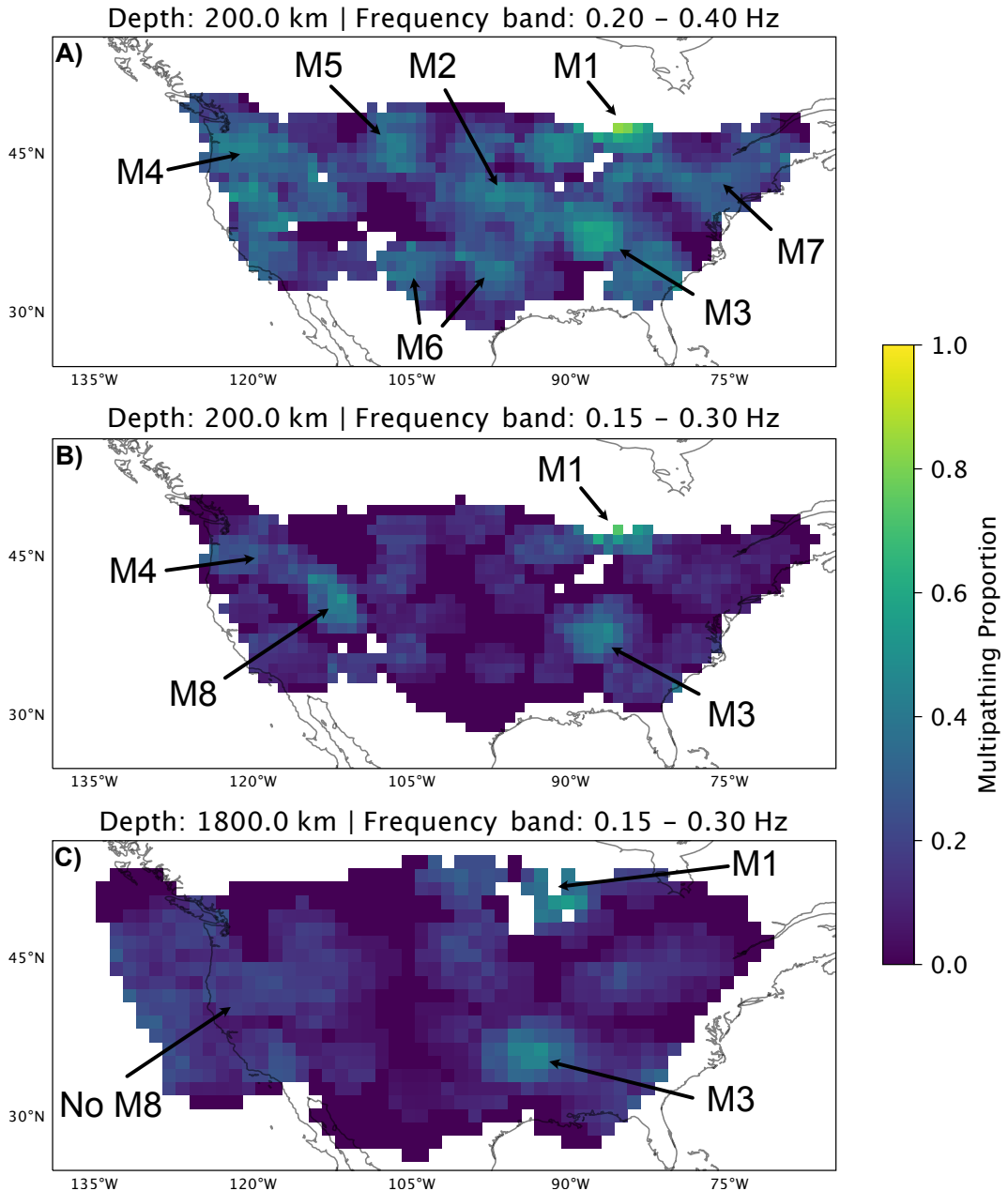


Figure 8. Proportion of multipathing observations relative to the total number of observations per bin. The sub-figures show different depth slices and frequency bands. A) 200 km depth and band 0.20 – 0.40 Hz, B) 200 km and band 0.15 – 0.30 Hz, C) 1800 km depth and band 0.15 – 0.30 Hz. This highlights the difference in the distribution of multipathing in the upper mantle between frequency bands (A and B) and the disappearance of multipathing proportion M8 with depth (B and C). Bins for the multipathing proportion measurements are 200 km radius, spaced with increments of 100 km.

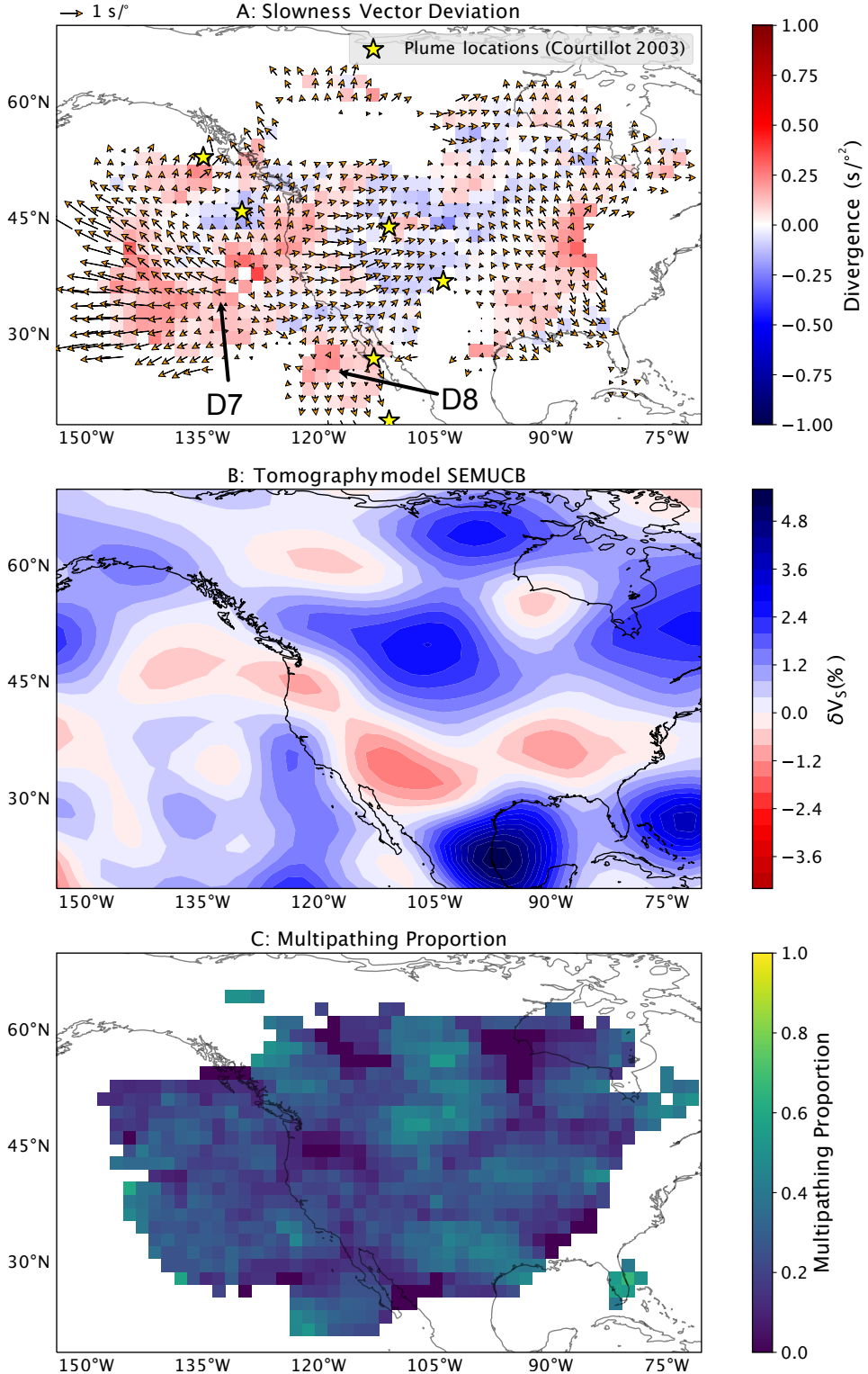


Figure 9. Figure of a) slowness vector deviation bins at 2891 km depth with the divergence in the background. Plume locations from Courtillot et al. (2003) are shown as yellow stars. The background shows the divergence of the slowness deviation vector field calculated using Equation 3. b) velocity structure of tomography model SEMUCB (French & Romanowicz, 2014) at 2891 km depth, and c) multipathing proportions in the 0.20 – 0.40 Hz frequency band using pierce points at 2891 km depth beneath the US. The bins have a radius of 200 km with a spacing of 100 km.

541 Figure 10 presents the slowness vector bins at 200 km depth where the variance
 542 analysis suggests most of the signal is being caused by structures at this depth. Visual
 543 inspection of Figure 10 shows the results from all models are able to reproduce the gen-
 544 eral structure of the data but all show differences on a finer scale. The CSEM model (Fichtner
 545 et al., 2018) was made using full waveform inversion (FWI) and, in theory, could use the
 546 same information as this study to create their velocity model. We argue using slowness
 547 vector measurements as we have here is still useful due to the higher frequencies usable,
 548 the lower computational cost and are able to use noisier data. Our preferred model is
 549 NA13 (Bedle et al., 2021) as it recovers the same converging and diverging patterns bet-
 550 ter than the CSEM model (Fichtner et al., 2018) and has more realistic slowness vec-
 551 tor deviation magnitudes than US-SL (Schmandt & Lin, 2014). There are differences with
 552 the observations still where the model produces lower magnitude slowness vector devi-
 553 tions indicating structure is not resolved by the tomography model. The differences show
 554 there is information in our observations about mantle structure not included in the to-
 555 mography and therefore the value of analysing the mantle using slowness vector mea-
 556 surements.

557 As lower mantle structure is not present in the models we can infer the effect of
 558 upper mantle structure on our observations of lower mantle structure. We find that the
 559 signal for all three models in the lowermost mantle is similar to that in the observations
 560 (Figure 11). Therefore, we conclude the apparent signal in the lowermost is caused by
 561 heterogeneity in the upper mantle beneath the US.

562 5 Geological interpretation

563 Our slowness vector deviation observations agree well with the velocity structure
 564 of tomography model NA13 (Bedle et al., 2021) and as such our interpretation of the seis-
 565 mically slow and fast anomaly locations would be similar. Multipathing provides differ-
 566 ent information to the slowness vector measurement and tomography studies. Multipathing
 567 is indicative of sharp lateral velocity gradients and the frequency band in which multi-
 568 pathing is observed can give further information on the spatial scales at which the gra-
 569 dient exists. Therefore, we focus our interpretation on the meaning of our multipathing
 570 observations in the context of the origin and nature of possible mantle upwellings and
 571 the origin of the seismically fast material we observe.

572 5.1 Upwellings beneath the US

573 In our interpretation, we assume the seismically slow regions identified are likely
 574 to be hot and therefore have a positive buoyancy and likely to be upwellings. From our
 575 divergence maps, we observe four regions of diverging slowness vector deviations which
 576 we interpret as upwellings beneath Yellowstone (D1), Appalachian mountains (D5), be-
 577 beneath the Colorado plateau (D3) and beneath southwest Utah (D2). These anomalies
 578 show unique multipathing behaviour.

579 5.1.1 Yellowstone

580 The Yellowstone anomaly is a heavily studied region of intra-plate volcanism with
 581 some controversy over its origin. Some suggest it is of shallow origin (Christiansen et al.,
 582 2002; Leonard & Liu, 2016) while others have suggested a deeply rooted plume (Nelson
 583 & Grand, 2018). Our observations are unable to determine if there is a lower mantle root
 584 as our lower mantle observations are strongly contaminated by signal in the upper man-
 585 tle. The Yellowstone anomaly is often observed to have the seismically slowest anomaly
 586 in tomography models (e.g., Bedle et al., 2021; Schmandt et al., 2012) and the temper-
 587 atures inferred from these anomalies are greater than the melting point of peridotite at
 588 50–100 km depth (Goes & Lee, 2002). Therefore, it is argued the Yellowstone anomaly

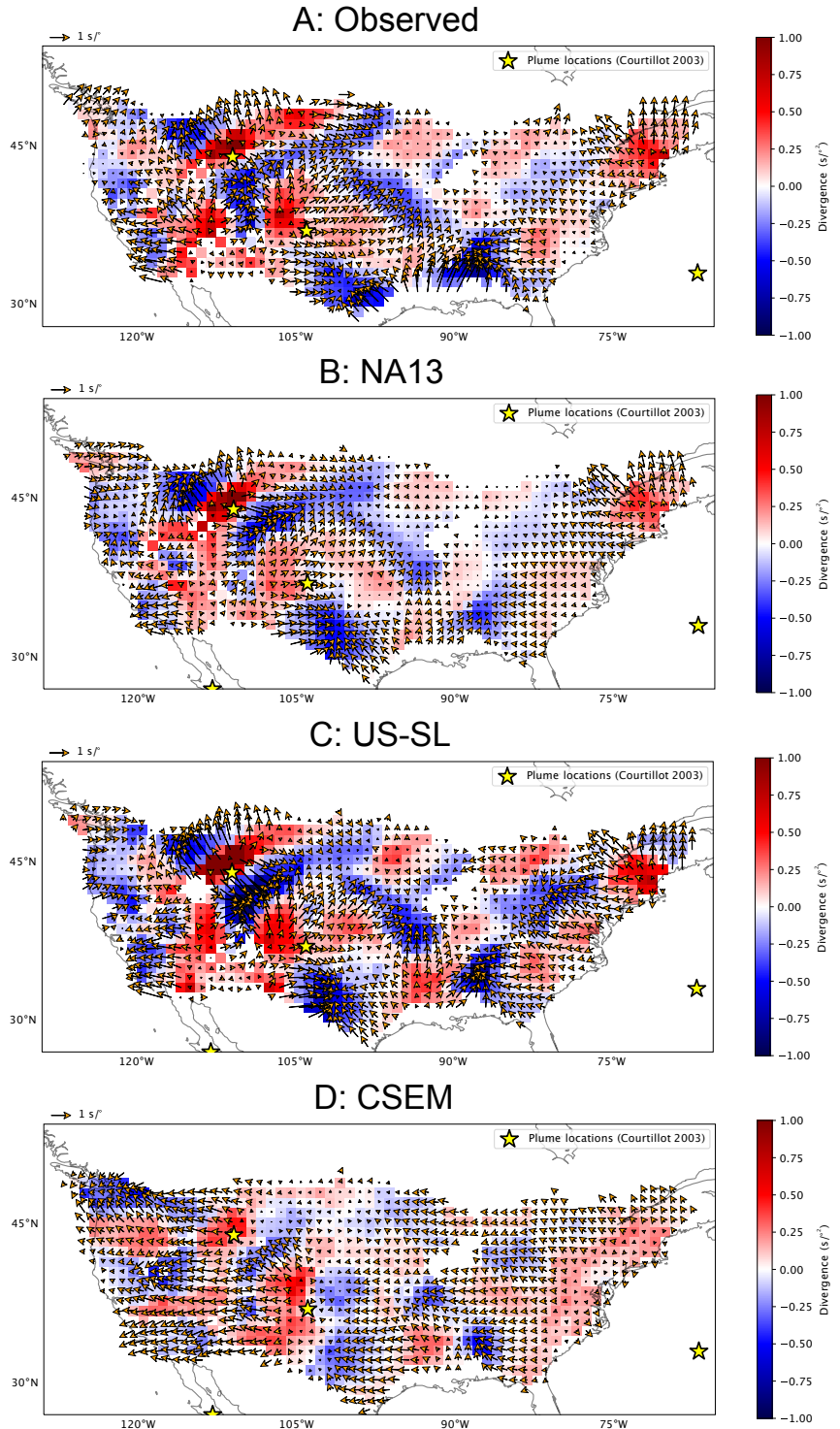


Figure 10. A comparison of a) observed slowness vector deviation bins with the divergence in the background at 200 km depth, b) synthetic results of the ray tracing using tomography model NA13 (Bedle et al., 2021) at 200 km depth, c) tomography model US-SL (Schmandt & Lin, 2014), and d) tomography model CSEM (Fichtner et al., 2018) at 200 km depth beneath the US. The bins have a radius of 200 km with a spacing of 100 km. plume locations from Courtillot et al. (2003) are shown as yellow stars. Background for each of the plots shows the divergence of the slowness deviation vector field calculated using Equation 3.

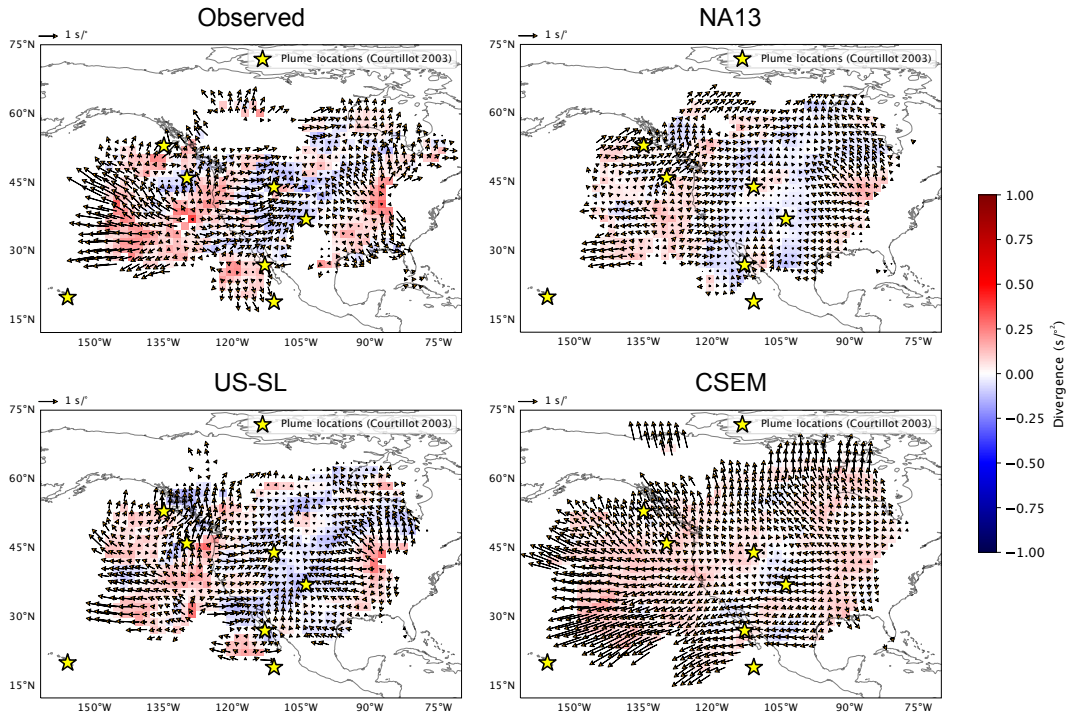


Figure 11. A comparison of the observed slowness vector deviation bins and divergence at 2891 km depth (a) with the results of ray tracing from the tomography models discussed. These tomography models have no lower mantle structures and so are a good test of the effect of upper mantle structure when trying to infer potential lower mantle heterogeneities. The models are NA13 (Bedle et al., 2021) (b), tomography model US-SL (Schmandt & Lin, 2014) (c) and tomography model CSEM (Fichtner et al., 2018) (d) all projected to 2891 km depth beneath the US. The bins have a radius of 200 km with a spacing of 100 km. plume locations from Courtillot et al. (2003) are shown as yellow stars. Background for each of the plots shows the divergence of the slowness deviation vector field calculated using Equation 3.

589 is home to partial melt. Observations of attenuation suggest the upper 200 km beneath
 590 Yellowstone attenuates more strongly than deeper in the mantle and could be more hy-
 591 drated (Adams & Humphreys, 2010). V_P/V_S ratios from tomography models agree the
 592 upper 200 km is distinct from deeper and may contain partial melt and be hydrated (Schmandt
 593 & Humphreys, 2010).

594 We observe multipathing at high frequencies at the boundaries of the Yellowstone
 595 anomaly (M4 and M5, Figure 8a), indicative of sharp velocity gradients at the bound-
 596 aries and a distinct transition in composition or thermal properties. As previous stud-
 597 ies have suggested the presence of partial melt in this region, we hypothesise the mul-
 598 tipathing could be caused by a transition from a region with partial melt and high tem-
 599 peratures to a colder region without partial melt. Using the approach outlined in Sec-
 600 tion 2.4 we estimate the maximum transition length would be approximately 470 km.

601 5.1.2 Small-Scale Upwellings

602 In addition to the Yellowstone anomaly, we interpret slowness vector deviations as
 603 evidence for smaller-scale low-velocity anomalies in the upper mantle as observed in pre-
 604 vious studies (Xue & Allen, 2007; Schmandt & Humphreys, 2010; Gilbert et al., 2003;
 605 Eagar et al., 2010), labeled D2 and D3 in Figure 7. The D2 pattern is located east of
 606 where previous studies identify a ‘slab window’ (Sigloch et al., 2008; Porritt et al., 2014;
 607 Tian et al., 2011) where the Farallon slab may have broken apart, possibly initiating small-
 608 scale upwelling from hydration melting and partial melt (Schmandt & Humphreys, 2010;
 609 Schmandt et al., 2012; Tian et al., 2009; Cao & Levander, 2010). We observe diverging
 610 region D3 which is possibly an upwelling to the east of the slab window. This region has
 611 a low multipathing proportion (Figure 8), counter to what we observe beneath Yellow-
 612 stone. The difference could be due to differences in velocity gradients or depth extents
 613 of the structures.

614 5.1.3 North Appalachian Anomaly

615 The North Appalachian anomaly (NAA) has been imaged in several tomography
 616 models (e.g., Schmandt & Lin, 2014; Yang & Gao, 2018; Bedle et al., 2021; Zhou et al.,
 617 2022), spans over 400 km in diameter and is thought to have very low seismic velocities
 618 of approximately -10% in V_S (Rychert et al., 2007; Menke et al., 2016). Some associate
 619 it with the Great Meteor hotspot (Taylor & Fitzgerald, 2011), but this may be the re-
 620 sult of a coincidental geometry (Menke et al., 2016). The anomaly has been hypothe-
 621 sised to be related to lithosphere delamination (G. A. Houseman & Molnar, 1997; G. House-
 622 man & Molnar, 2001). Our multipathing observations show a small proportion in the
 623 high-frequency band suggesting the anomaly transitions over a distance of at most 470 km.
 624 Any future hypotheses of the cause of this structure will need to be able to have suffi-
 625 ciently sharp boundaries to satisfy our observations.

626 5.2 Upper mantle fast seismic anomalies

627 The subduction history of the US is still a region of active debate and discussion,
 628 largely due to the complexity of mantle structure and how these structures interact. The
 629 upper mantle in the west can be broadly characterised as a large region of low velocity
 630 with high-velocity structures scattered throughout (Porritt et al., 2014; Schmandt & Lin,
 631 2014; Fichtner et al., 2018). This, with observations of a thin low-velocity zone above
 632 the mantle transition zone at 410 km depth (Gao et al., 2006; Vinnik et al., 2010; Schmandt
 633 et al., 2011; Song et al., 2004), is interpreted as the Farallon slab subducting into the up-
 634 per mantle, releasing water and causing partial melt and small-scale upwellings in the
 635 upper mantle (Schmandt & Humphreys, 2010; Schmandt et al., 2012; Tian et al., 2009;
 636 Cao & Levander, 2010). The Yellowstone plume is speculated to affect the Farallon slab
 637 by causing tears and gaps in the slab observed as patches of high-velocity regions (Sigloch

et al., 2008; Tian et al., 2011; Pierce & Morgan, 2009; Obrebski et al., 2010; Xue & Allen, 2007; Leonard & Liu, 2016). Seismically fast material observed further to the east has been interpreted as lithospheric material with much discussion on its origin (Liu et al., 2010; Biryol et al., 2016; Wang et al., 2019). Like many tomography studies, we observe several seismically fast anomalies throughout the upper mantle. These fast anomalies show very different multipathing observations and in this section, we interpret these in the context of their subduction history.

645 5.2.1 Cascadia

646 Some tomography studies observe seismically fast material along the Cascadia sub-
 647 duction margin on the west coast of the US with a possible gap between the Juan de Fuca
 648 and Gorda slab (e.g. Bedle et al., 2021; Schmandt & Lin, 2014), which some suggest may
 649 be due to slab break off (Obrebski et al., 2011). The presence of this window is debated
 650 with some arguing it is an imaging artifact due to resolution limitations of the tomographic
 651 approaches (Roth et al., 2008) or affected by the starting velocity model (Long, 2016).
 652 Other studies have presented observations supportive of a continuous slab without a win-
 653 dow with reflectors (Tauzin et al., 2016) and episodic tremor and slip (Audet et al., 2010).
 654 Our observations show multipathing is present all along the west coast of the US (M4,
 655 Figure 8a) at high frequencies which is compatible with both the broken and intact slab
 656 hypotheses.

657 5.2.2 Mid-Mantle Slabs

658 We observe evidence for seismically fast anomalies beneath the eastern US (C3 and
 659 C4) and where we observe multipathing regions M2 and M3. There is much speculation
 660 on the origin of the C4 anomaly, where we observe evidence for a fast anomaly agree-
 661 ing with several tomography models (Schmandt et al., 2011; Schmandt & Lin, 2014; Por-
 662 rritt et al., 2014; Sigloch et al., 2008). Some suggest it could be a Farallon slab fragment
 663 of age 40 Ma which has stagnated above the 660 km transition (Sigloch et al., 2008; Liu
 664 & Stegman, 2011). Other suggest it could be a Grenville slab fragment again stagnat-
 665 ing in the mid-mantle. Some find by inverse convection models and plate reconstruc-
 666 tion models that these align palaeogeographically with the Shatsky and Hess conjugate plateau
 667 as they subducted beneath North America (Liu et al., 2010). All of these require a mech-
 668 anism for slab stagnation where other slabs have descended deeper. As neither are at-
 669 tached to the crust some mechanism for neutral buoyancy or a barrier at 660 km is needed.
 670 Alternatively, there is a suggestion of dense lithosphere delamination or a dripping pro-
 671 cess where lithosphere drops into the mantle by a Raleigh-Taylor instability (Biryol et
 672 al., 2016; G. A. Houseman & Molnar, 1997).

673 Like the C4 anomaly in the east, we observe a distinct region of multipathing in
 674 the central frequency band (0.15 – 0.30 Hz) near anomalies C2 southeast of Yellowstone
 675 (Figure 7a). We interpret this as the boundaries of the C4 and C2 heterogeneities hav-
 676 ing a large velocity contrast and also transitioning over a longer distance. These anom-
 677 alies have been imaged as fast anomalies between the 410 km and 660 km deep transi-
 678 tion zone in several tomography models (Sigloch et al., 2008; Schmandt & Lin, 2014; Por-
 679 rritt et al., 2014; Wang et al., 2019; Bedle et al., 2021). We interpret this as possible litho-
 680 sphere which has descended into the mid mantle and is sufficiently old that it has been
 681 heated by the mantle and has weaker thermal gradients at its boundaries. These weaker
 682 gradients are able to produce multipathing in the central frequency band and we esti-
 683 mate the transition length of the boundaries is at most 510 km.

684 6 Future work

685 The results presented in this study show continent-scale observations of slowness
 686 vector deviations and multipathing can be made automatically, can resolve seismically
 687 slow and fast anomalies and identify sharp boundaries not easily resolved by tomogra-
 688 phy models. Better imaging can be achieved by extending the analysis to include direct
 689 arrivals, core reflected waves, core diffracted and other core refracted phases. This would
 690 then further constrain the location of mantle heterogeneity and sharp velocity gradients.
 691 As discussed above, some heterogeneities previously observed as fast anomalies within
 692 the transition zone (410 to 660 km depth) show high proportions of multipathing in the
 693 central frequency band (Figure 8). We speculate this may be due to weaker velocity gra-
 694 dients around the slab as it passes through the mantle and warms. Using multipathing
 695 signatures of fast seismic anomalies may be able to give more information on their ther-
 696 mal state and contribute to the question of why some stagnate while others do not. As
 697 each heterogeneity seemingly has a unique combination of multipathing and slowness vec-
 698 tor observations, forward modelling could effectively constrain the morphology, veloc-
 699 ity gradient properties and velocity perturbation of these anomalies with care taken to
 700 account for dipping boundaries (Niazi, 1966).

701 Slowness vector measurements can be made automatically on a continental scale
 702 and larger. These measurements are not currently included in a tomographic inversion,
 703 but we now argue these provide complementary information to travel times and could
 704 improve the resolution in the inversion. In the forward modelling, the velocity vector could
 705 be measured at the points where the slowness vector measurements are made by taking
 706 the spatial derivative of the travel times. This would then provide a suitable compar-
 707 ison that can be iteratively reduced in an inversion setup. As the slowness vector mea-
 708 surements were made using beamforming described earlier, they are sensitive to frequency
 709 and waveform information that travel time tomography is not. Furthermore, array-based
 710 methods can be used to identify paths where multipathing occurs which travel time to-
 711 mography is not sensitive to. By adding slowness vector observations as a constraint, we
 712 argue tomographic inversions will be able to better resolve mantle heterogeneity.

713 7 Conclusions

714 We have presented the first continent-scale dataset quantifying the deflection of tele-
 715 seismic shear waves and multipathing caused by mantle heterogeneity. This study shows
 716 this scale of dataset and larger can be created automatically. Our observations provide
 717 insight into the lateral velocity gradients throughout the mantle beneath the US, giv-
 718 ing information on thermal or chemical gradients in the mantle. We confirm a frequency
 719 dependence of observable multipathing, observe a frequency dependence of slowness vec-
 720 tor deviation magnitudes and show the divergence or convergence of the slowness vec-
 721 tor deviation field can image fast and slow heterogeneity well. Multipathing in different
 722 frequency bands can be used to identify structures in the mantle. High-frequency mul-
 723 tipathing observed widely across the upper mantle suggests velocity gradients are present
 724 with length scales of up to 470 km, but constraining the depths of SKS multipathing is
 725 challenging. Multipathing in the central frequency band is observed in local regions where
 726 fast anomalies have been observed in the mantle transition zone (e.g. Sigloch et al., 2008).
 727 We interpret these anomalies as being older than the other fast anomalies and have been
 728 warmed by the mantle, leading to weaker velocity gradients at their boundaries. By com-
 729 paring our results to those created using ray-tracing through tomography models, we find
 730 our results are best replicated by model NA13 (Bedle et al., 2021) showing that slow-
 731 ness vector measurements are effective in resolving mantle structure. The differences be-
 732 tween the observed and synthetic data show slowness vector measurements provide more
 733 constraints on mantle structure which could be incorporated into tomographic inversions.

734 8 Open Research

735 The processed seismograms used to make the array measurements are stored as SAC
736 (Goldstein et al., 2003) files are freely available on figshare via [10.6084/m9.figshare
737 .21701621](https://doi.org/10.6084/m9.figshare.21701621) under a CC BY 4.0 license with a list of events used here [10.6084/m9.figshare
738 .21710564](https://doi.org/10.6084/m9.figshare.21710564). The data is taken as a subset from Thorne et al. (2020) which was collected
739 using the SOD software (Owens et al., 2004) and the raw seismograms are freely avail-
740 able from the IRIS Data Management Centre with the dois for each network used pro-
741 vided in the supplementary material. Figures were made using Matplotlib (Hunter, 2007)
742 and cartopy (Met Office, 2010 - 2015). Travel time and slowness predictions from 1D ve-
743 locity models were made using the TauP toolkit (Crotwell et al., 1999). Code to make
744 automated slowness vector measurements is publicly available from [https://github.com/
745 eejwa/Array_Seis_Circle](https://github.com/eejwa/Array_Seis_Circle).

746 Acknowledgments

747 We thank the reviewers for taking the time to read and suggest corrections that improved
748 the manuscript. JW is supported by the NERC DTP SPHERES grant NE/L002574/1,
749 AN was funded by NERC standard grant NE/R001154/1 (REMIS: Reliable Earthquake
750 Magnitudes for Induced Seismicity), AN and JW are supported by NERC large grant
751 Mantle Circulation Constrained NE/T012684/1, SR was supported by NE/R012199/1
752 and MT was partially supported by NSF grant EAR-1723081.

753 References

- 754 Abt, D. L., Fischer, K. M., French, S. W., Ford, H. A., Yuan, H., & Romanowicz, B.
 755 (2010). North American lithospheric discontinuity structure imaged by Ps and
 756 Sp receiver functions. *Journal of Geophysical Research: Solid Earth*, 115(B9).
- 757 Adams, D. C., & Humphreys, E. D. (2010). New constraints on the properties of the
 758 Yellowstone mantle plume from P and S wave attenuation tomography. *Journal
 759 of Geophysical Research: Solid Earth*, 115(B12).
- 760 Audet, P., Bostock, M. G., Boyarko, D. C., Brudzinski, M. R., & Allen, R. M.
 761 (2010). Slab morphology in the Cascadia fore arc and its relation to episodic
 762 tremor and slip. *Journal of Geophysical Research: Solid Earth*, 115(B4).
- 763 Bedle, H., Lou, X., & Van der Lee, S. (2021). Continental Tectonics Inferred From
 764 High-Resolution Imaging of the Mantle Beneath the United States, Through
 765 the Combination of USArray Data Types. *Geochemistry, Geophysics, Geosys-
 766 tems*, 22(10), e2021GC009674.
- 767 Benton, H. L. M., Rost, S., & Thorne, M. S. (2017, August). Fine-scale structure
 768 of the mid-mantle characterised by global stacks of PP precursors. *Earth and
 769 Planetary Science Letters*, 472, 164–173.
- 770 Biryol, C. B., Wagner, L. S., Fischer, K. M., & Hawman, R. B. (2016). Relationship
 771 between observed upper mantle structures and recent tectonic activity across
 772 the southeastern United States. *Journal of Geophysical Research: Solid Earth*,
 773 121(5), 3393–3414.
- 774 Bunge, H.-P., & Grand, S. P. (2000, May). Mesozoic plate-motion history below the
 775 northeast Pacific Ocean from seismic images of the subducted Farallon slab.
 776 *Nature*, 405(6784), 337–340.
- 777 Cao, A., & Levander, A. (2010). High-resolution transition zone structures of the
 778 Gorda Slab beneath the western United States: Implication for deep water
 779 subduction. *Journal of Geophysical Research: Solid Earth*, 115(B7).
- 780 Capon, J. (1974). Characterization of crust and upper mantle structure under LASA
 781 as a random medium. *Bulletin of the Seismological Society of America*, 64(1),
 782 235–266.
- 783 Christiansen, R. L., Foulger, G., & Evans, J. R. (2002). Upper-mantle origin of the
 784 Yellowstone hotspot. *Geological Society of America Bulletin*, 114(10), 1245–
 785 1256.
- 786 Courtillot, V., Davaille, A., Besse, J., & Stock, J. (2003, January). Three distinct
 787 types of hotspots in the Earth's mantle. *Earth and Planetary Science Letters*,
 788 205(3), 295–308.
- 789 Crotwell, H. P., Owens, T. J., & Ritsema, J. (1999). The TauP Toolkit: Flexi-
 790 ble seismic travel-time and ray-path utilities. *Seismological Research Letters*,
 791 70(2), 154–160.
- 792 Deuss, A. (2009, October). Global Observations of Mantle Discontinuities Using SS
 793 and PP Precursors. *Surveys in Geophysics*, 30(4-5), 301–326.
- 794 Deuss, A., Redfern, S. A. T., Chambers, K., & Woodhouse, J. H. (2006, January).
 795 The Nature of the 660-Kilometer Discontinuity in Earth's Mantle from Global
 796 Seismic Observations of PP Precursors. *Science*, 311(5758), 198–201.
- 797 Dziewonski, A. M., & Anderson, D. L. (1981). Preliminary reference Earth model.
 798 *Physics of the earth and planetary interiors*, 25(4), 297–356.
- 799 Eagar, K. C., Fouch, M. J., & James, D. E. (2010, August). Receiver function imag-
 800 ing of upper mantle complexity beneath the Pacific Northwest, United States.
 801 *Earth and Planetary Science Letters*, 297(1), 141–153.
- 802 Efron, B. (1992). Bootstrap Methods: Another Look at the Jackknife. In S. Kotz &
 803 N. L. Johnson (Eds.), *Breakthroughs in Statistics: Methodology and Distribu-
 804 tion* (pp. 569–593). New York, NY: Springer.
- 805 Ester, M., Kriegel, H.-P., Sander, J., Xu, X., & others. (1996). A density-based al-
 806 gorithm for discovering clusters in large spatial databases with noise. In *Kdd*
 807 (Vol. 96, pp. 226–231).

- 808 Fichtner, A., van Herwaarden, D.-P., Afanasiev, M., Simutė, S., Krischer, L., Çubuk
 809 Sabuncu, Y., ... Igel, H. (2018). The Collaborative Seismic Earth Model:
 810 Generation 1. *Geophysical Research Letters*, 45(9), 4007–4016.
- 811 French, S., & Romanowicz, B. (2014). Whole-mantle radially anisotropic shear veloc-
 812 ity structure from spectral-element waveform tomography. *Geophysical Journal
 813 International*, 199(3), 1303–1327.
- 814 Gao, W., Matzel, E., & Grand, S. P. (2006). Upper mantle seismic structure be-
 815 neath eastern Mexico determined from P and S waveform inversion and its
 816 implications. *Journal of Geophysical Research: Solid Earth*, 111(B8).
- 817 Gilbert, H. J., Sheehan, A. F., Dueker, K. G., & Molnar, P. (2003). Receiver func-
 818 tions in the western United States, with implications for upper mantle struc-
 819 ture and dynamics. *Journal of Geophysical Research: Solid Earth*, 108(B5).
- 820 Goes, S., & Lee, S. v. d. (2002). Thermal structure of the North American up-
 821 permost mantle inferred from seismic tomography. *Journal of Geophysical Re-
 822 search: Solid Earth*, 107(B3), ETG 2–1–ETG 2–13.
- 823 Goldstein, P., Dodge, D., Firpo, M., Minner, L., Lee, W., Kanamori, H., ...
 824 Kisslinger, C. (2003). SAC2000: Signal processing and analysis tools for
 825 seismologists and engineers. *The IASPEI international handbook of earthquake
 826 and engineering seismology*, 81, 1613–1620.
- 827 Grand, S. P., van der Hilst, R. D., & Widjiantoro, S. (1997). High resolution global
 828 tomography: a snapshot of convection in the Earth. *Geological Society of
 829 America Today*, 7(4).
- 830 Hedlin, M. A. H., & Shearer, P. M. (2000). An analysis of large-scale variations in
 831 small-scale mantle heterogeneity using Global Seismographic Network record-
 832 ings of precursors to PKP. *Journal of Geophysical Research: Solid Earth*,
 833 105(B6), 13655–13673.
- 834 Houseman, G., & Molnar, P. (2001). Mechanisms of lithospheric rejuvenation as-
 835 sociated with continental orogeny. *Geological Society, London, Special Publica-
 836 tions*, 184(1), 13–38.
- 837 Houseman, G. A., & Molnar, P. (1997). Gravitational (Rayleigh–Taylor) instabil-
 838 ity of a layer with non-linear viscosity and convective thinning of continental
 839 lithosphere. *Geophysical Journal International*, 128(1), 125–150.
- 840 Hunter, J. D. (2007). Matplotlib: A 2D graphics environment. *Computing in Science
 841 & Engineering*, 9(3), 90–95. doi: 10.1109/MCSE.2007.55
- 842 Jenkins, J., Deuss, A., & Cottaar, S. (2017, February). Converted phases from sharp
 843 1000 km depth mid-mantle heterogeneity beneath Western Europe. *Earth and
 844 Planetary Science Letters*, 459, 196–207.
- 845 Kennett, B., Engdahl, E., & Buland, R. (1995). Constraints on seismic velocities
 846 in the Earth from traveltimes. *Geophysical Journal International*, 122(1), 108–
 847 124.
- 848 Kind, R., Yuan, X., Mechier, J., & Sodoudi, F. (2015). Structure of the upper man-
 849 ttle in the north-western and central United States from USArray S-receiver
 850 functions. *Solid Earth*, 6(3), 957–970.
- 851 Krischer, L., Fichtner, A., Boehm, C., & Igel, H. (2018). Automated large-scale full
 852 seismic waveform inversion for North America and the North Atlantic. *Journal
 853 of Geophysical Research: Solid Earth*, 123(7), 5902–5928.
- 854 Leonard, T., & Liu, L. (2016). The role of a mantle plume in the formation of Yel-
 855 lowstone volcanism. *Geophysical Research Letters*, 43(3), 1132–1139.
- 856 Liu, L., Gurnis, M., Seton, M., Saleeby, J., Müller, R. D., & Jackson, J. M. (2010).
 857 The role of oceanic plateau subduction in the Laramide orogeny. *Nature Geo-
 858 science*, 3(5), 353–357.
- 859 Liu, L., & Stegman, D. R. (2011). Segmentation of the Farallon slab. *Earth and
 860 Planetary Science Letters*, 311(1-2), 1–10.
- 861 Long, M. D. (2016). The Cascadia Paradox: Mantle flow and slab fragmentation in
 862 the Cascadia subduction system. *Journal of Geodynamics*, 102, 151–170.

- 863 Ma, X., & Thomas, C. (2020). Small-Scale Scattering Heterogeneities in the Lower-
 864 most Mantle From a Global Analysis of PKP Precursors. *Journal of Geophysical*
 865 *Research: Solid Earth*, *125*(3), e2019JB018736.
- 866 Maupin, V. (2011). Upper-mantle structure in southern Norway from beamform-
 867 ing of Rayleigh wave data presenting multipathing. *Geophysical Journal Interna-*
 868 *tional*, *185*(2), 985–1002.
- 869 Menke, W., Skryzalin, P., Levin, V., Harper, T., Derbyshire, F., & Dong, T. (2016).
 870 The Northern Appalachian Anomaly: A modern asthenospheric upwelling.
 871 *Geophysical Research Letters*, *43*(19), 10,173–10,179.
- 872 Met Office. (2010 - 2015). Cartopy: a cartographic python library with a Mat-
 873plotlib interface [Computer software manual]. Exeter, Devon. Retrieved from
 874 <https://scitools.org.uk/cartopy>
- 875 Nelson, P. L., & Grand, S. P. (2018, April). Lower-mantle plume beneath the Yel-
 876 lowstone hotspot revealed by core waves. *Nature Geoscience*, *11*(4), 280–284.
- 877 Ni, S., & Helmberger, D. V. (2003). Ridge-like lower mantle structure beneath south
 878 Africa. *Journal of Geophysical Research: Solid Earth*, *108*(B2).
- 879 Ni, S., Tan, E., Gurnis, M., & Helmberger, D. (2002). Sharp sides to the African su-
 880 perplume. *Science*, *296*(5574), 1850–1852.
- 881 Niazi, M. (1966). Corrections to apparent azimuths and travel-time gradients for
 882 a dipping Mohorovičić discontinuity. *Bulletin of the Seismological Society of*
 883 *America*, *56*(2), 491–509.
- 884 Obrebski, M., Allen, R. M., Pollitz, F., & Hung, S.-H. (2011). Lithosphere–
 885 asthenosphere interaction beneath the western United States from the joint
 886 inversion of body-wave traveltimes and surface-wave phase velocities. *Geophys-*
 887 *ical Journal International*, *185*(2), 1003–1021.
- 888 Obrebski, M., Allen, R. M., Xue, M., & Hung, S.-H. (2010). Slab-plume interaction
 889 beneath the Pacific Northwest. *Geophysical Research Letters*, *37*(14).
- 890 Owens, T. J., Crotwell, H. P., Groves, C., & Oliver-Paul, P. (2004). SOD: Standing
 891 order for data. *Seismological Research Letters*, *75*(4), 515–520.
- 892 Pierce, K. L., & Morgan, L. A. (2009, November). Is the track of the Yellowstone
 893 hotspot driven by a deep mantle plume? — Review of volcanism, faulting, and
 894 uplift in light of new data. *Journal of Volcanology and Geothermal Research*,
 895 *188*(1), 1–25.
- 896 Porritt, R. W., Allen, R. M., & Pollitz, F. F. (2014, September). Seismic imaging
 897 east of the Rocky Mountains with USArray. *Earth and Planetary Science Let-*
 898 *ters*, *402*, 16–25.
- 899 Ricker, N. (1943). Further developments in the wavelet theory of seismogram struc-
 900 *ture*. *Bulletin of the Seismological Society of America*, *33*(3), 197–228.
- 901 Ricker, N. (1944). Wavelet functions and their polynomials. *Geophysics*, *9*(3), 314–
 902 323.
- 903 Ritsema, J., Kaneshima, S., & Haugland, S. M. (2020, September). The dimen-
 904 sions of scatterers in the lower mantle using USArray recordings of S-wave
 905 to P-wave conversions. *Physics of the Earth and Planetary Interiors*, *306*,
 906 106541.
- 907 Rodgers, A., Krischer, L., Afanasiev, M., Boehm, C., Doody, C., Chiang, A., &
 908 Simmons, N. (2022). WUS256: An Adjoint Waveform Tomography Model
 909 of the Crust and Upper Mantle of the Western United States for Improved
 910 Waveform Simulations. *Journal of Geophysical Research: Solid Earth*, *127*(7),
 911 e2022JB024549.
- 912 Rost, S., & Thomas, C. (2002). Array seismology: Methods and applications. *Re-*
 913 *views of geophysics*, *40*(3).
- 914 Roth, J. B., Fouch, M. J., James, D. E., & Carlson, R. W. (2008). Three-
 915 dimensional seismic velocity structure of the northwestern United States.
 916 *Geophysical Research Letters*, *35*(15).
- 917 Rychert, C. A., Rondenay, S., & Fischer, K. M. (2007). P-to-S and S-to-P imaging

- of a sharp lithosphere-asthenosphere boundary beneath eastern North America. *Journal of Geophysical Research: Solid Earth*, 112(B8).
- Schmandt, B., Dueker, K., Humphreys, E., & Hansen, S. (2012, May). Hot mantle upwelling across the 660 beneath Yellowstone. *Earth and Planetary Science Letters*, 331-332, 224–236.
- Schmandt, B., Dueker, K. G., Hansen, S. M., Jasbinsek, J. J., & Zhang, Z. (2011). A sporadic low-velocity layer atop the western U.S. mantle transition zone and short-wavelength variations in transition zone discontinuities. *Geochemistry, Geophysics, Geosystems*, 12(8).
- Schmandt, B., & Humphreys, E. (2010, September). Complex subduction and small-scale convection revealed by body-wave tomography of the western United States upper mantle. *Earth and Planetary Science Letters*, 297(3), 435–445.
- Schmandt, B., Jacobsen, S. D., Becker, T. W., Liu, Z., & Dueker, K. G. (2014). Dehydration melting at the top of the lower mantle. *Science*, 344(6189), 1265–1268.
- Schmandt, B., & Lin, F.-C. (2014). P and S wave tomography of the mantle beneath the United States. *Geophysical Research Letters*, 41(18), 6342–6349.
- Shen, W., & Ritzwoller, M. H. (2016). Crustal and uppermost mantle structure beneath the United States. *Journal of Geophysical Research: Solid Earth*, 121(6), 4306–4342.
- Sigloch, K., McQuarrie, N., & Nolet, G. (2008, July). Two-stage subduction history under North America inferred from multiple-frequency tomography. *Nature Geoscience*, 1(7), 458–462.
- Simmons, N., Myers, S., & Johannesson, G. (2011). Global-scale P wave tomography optimized for prediction of teleseismic and regional travel times for Middle East events: 2. Tomographic inversion. *Journal of Geophysical Research: Solid Earth*, 116(B4).
- Simmons, N., Myers, S. C., Johannesson, G., & Matzel, E. (2012). LLNL-G3Dv3: Global P wave tomography model for improved regional and teleseismic travel time prediction. *Journal of Geophysical Research: Solid Earth*, 117(B10).
- Song, A. T.-R., Helmberger, D. V., & Grand, S. P. (2004, February). Low-velocity zone atop the 410-km seismic discontinuity in the northwestern United States. *Nature*, 427(6974), 530–533.
- Sun, D., Helmberger, D., Lai, V. H., Gurnis, M., Jackson, J. M., & Yang, H.-Y. (2019, March). Slab Control on the Northeastern Edge of the Mid-Pacific LLSVP Near Hawaii. *Geophysical Research Letters*, 46(6), 3142–3152.
- Sun, D., Helmberger, D., Ni, S., & Bower, D. (2009, May). Direct measures of lateral velocity variation in the deep Earth. *Journal of Geophysical Research: Solid Earth*, 114(B5).
- Tao, Z., Li, A., & Fischer, K. M. (2020, December). Hotspot signatures at the North American passive margin. *Geology*, 49(5), 525–530.
- Tauzin, B., Bodin, T., Debayle, E., Perrillat, J.-P., & Reynard, B. (2016). Multi-mode conversion imaging of the subducted Gorda and Juan de Fuca plates below the North American continent. *Earth and Planetary Science Letters*, 440, 135–146.
- Taylor, J. P., & Fitzgerald, P. G. (2011). Low-temperature thermal history and landscape development of the eastern Adirondack Mountains, New York: Constraints from apatite fission-track thermochronology and apatite (U-Th)/He dating. *Bulletin*, 123(3-4), 412–426.
- Thorne, M. S., Leng, K., Pachhai, S., Rost, S., Wicks, J., & Nissen-Meyer, T. (2021). The Most Parsimonious Ultralow-Velocity Zone Distribution From Highly Anomalous SPdKS Waveforms. *Geochemistry, Geophysics, Geosystems*, 22(1), e2020GC009467.
- Thorne, M. S., Pachhai, S., Leng, K., Wicks, J. K., & Nissen-Meyer, T. (2020, March). New Candidate Ultralow-Velocity Zone Locations from Highly

- 973 Anomalous SPdKS Waveforms. *Minerals*, 10(3), 211.
- 974 Tian, Y., Sigloch, K., & Nolet, G. (2009, September). Multiple-frequency SH-wave
975 tomography of the western US upper mantle. *Geophysical Journal International*, 178(3), 1384–1402.
- 976 Tian, Y., Zhou, Y., Sigloch, K., Nolet, G., & Laske, G. (2011). Structure of North
977 American mantle constrained by simultaneous inversion of multiple-frequency
978 SH, SS, and Love waves. *Journal of Geophysical Research: Solid Earth*,
979 116(B2).
- 980 Valentine, A. P., & Woodhouse, J. H. (2010, August). Approaches to automated
981 data selection for global seismic tomography. *Geophysical Journal Interna-*
982 *tional*, 182(2), 1001–1012.
- 983 Vinnik, L. P., Oreshin, S. I., Speziale, S., & Weber, M. (2010). Mid-mantle layering
984 from SKS receiver functions. *Geophysical Research Letters*, 37(24).
- 985 Wang, H., Zhao, D., Huang, Z., & Wang, L. (2019). Tomography, seismotecton-
986 ics, and mantle dynamics of central and eastern United States. *Journal of Geo-*
987 *physical Research: Solid Earth*, 124(8), 8890–8907.
- 988 Ward, J., Nowacki, A., & Rost, S. (2020). Lateral Velocity Gradients in the African
989 Lower Mantle Inferred From Slowness Space Observations of Multipathing.
990 *Geochemistry, Geophysics, Geosystems*, 21(8), e2020GC009025.
- 991 Ward, J., Thorne, M., Nowacki, A., & Rost, S. (2021, September). Automatic slow-
992 ness vector measurements of seismic arrivals with uncertainty estimates using
993 bootstrap sampling, array methods and unsupervised learning. *Geophysical*
994 *Journal International*, 226(3), 1847–1857.
- 995 Waszek, L., Schmerr, N. C., & Ballmer, M. D. (2018, January). Global observa-
996 tions of reflectors in the mid-mantle with implications for mantle structure and
997 dynamics. *Nature Communications*, 9(1), 385.
- 998 Waszek, L., Thomas, C., & Deuss, A. (2015). PKP precursors: Implications for
999 global scatterers. *Geophysical Research Letters*, 42(10), 3829–3838.
- 1000 Xue, M., & Allen, R. M. (2007, December). The fate of the Juan de Fuca plate: Im-
1001 plications for a Yellowstone plume head. *Earth and Planetary Science Letters*,
1002 264(1), 266–276.
- 1003 Yang, X., & Gao, H. (2018). Full-wave seismic tomography in the northeastern
1004 United States: New insights into the uplift mechanism of the Adirondack
1005 Mountains. *Geophysical Research Letters*, 45(12), 5992–6000.
- 1006 Yuan, H., French, S., Cupillard, P., & Romanowicz, B. (2014, September). Litho-
1007 spheric expression of geological units in central and eastern North America
1008 from full waveform tomography. *Earth and Planetary Science Letters*, 402,
1009 176–186.
- 1010 Zhao, C., Garnero, E. J., McNamara, A. K., Schmerr, N., & Carlson, R. W. (2015).
1011 Seismic evidence for a chemically distinct thermochemical reservoir in Earth's
1012 deep mantle beneath Hawaii. *Earth and Planetary Science Letters*, 426, 143–
1013 153.
- 1014 Zhao, D., Hasegawa, A., & Horiuchi, S. (1992). Tomographic imaging of P and
1015 S wave velocity structure beneath northeastern Japan. *Journal of Geophysical*
1016 *Research: Solid Earth*, 97(B13), 19909–19928.
- 1017 Zhou, T., Li, J., Xi, Z., Li, G., & Chen, M. (2022). CUSRA2021: A Radially
1018 Anisotropic Model of the Contiguous US and Surrounding Regions by Full-
1019 Waveform Inversion. *Journal of Geophysical Research: Solid Earth*, 127(8),
1020 e2021JB023893.
- 1021